



Stressed microstructures in thermally induced M9R–M18R martensites

Xavier Balandraud^{a,*}, Giovanni Zanzotto^b

^a*Laboratoire de Mécanique et Ingénieries (LaMI), Institut Français de Mécanique Avancée (IFMA), Université Blaise Pascal (UBP), Campus de Clermont-Ferrand/les Cèzeaux, B.P. 265, 63175 Aubière Cedex, France*

^b*Dipartimento di Metodi e Modelli Matematici per le Scienze Applicate (DMMMSA), Università di Padova, Via Belzoni 7, 35131 Padova, Italy*

Received 3 May 2005; received in revised form 3 February 2006; accepted 31 March 2006

Dedicated to Prof. J.L. Ericksen on the occasion of his 80th birthday

Abstract

We revisit the phase transformation that produces ‘long-period stacking’ M9R–M18R martensites in Cu-based shape-memory alloys and analyze some associated microstructures, in particular, the typical wedge-shaped configuration. Our basic premise is that the cubic-to-monoclinic martensitic phase change in these alloys is, geometrically, but a slight modification of the well-known bcc-to-9R transformation occurring in various elemental crystals, whose lattice strain is, at the microlevel, the same Bain strain as for the bcc-to-fcc transformation. For the memory alloys we thus determine the ‘near-Bain’ microstrain, thereby analyzing the faulted, long-period stacking martensite as a mesoscale structure derived from compatibility with the austenite. We compute the transformation-twin systems, habit planes, average deformation and stacking-fault density of the 9R, 18R, M9R or M18R martensites, as they arise from the compatibility conditions between the parent and product lattices. We confirm earlier conclusions that a stress-free wedge is not kinematically compatible in these materials. However, we show that this microstructure is ‘close enough’ to compatibility, finding that its stress levels are low and should cause only minimal plastification and damage in the crystal. The wedge is therefore rationalized as a viable path for the transformation also in these substances. We verify this to hold for all the lattice parameters reported for Cu-based alloys. In general, we conclude that martensitic microstructures can be stressed to a degree also in good memory materials. Furthermore, we find that the lattice-parameter relations, guaranteeing the zero-stress compatibility of special configurations favoring the transformation and its reversibility, do not need to be strictly

*Corresponding author.

E-mail addresses: xavier.balandraud@ifma.fr (X. Balandraud), zanzotto@dmsa.unipd.it (G. Zanzotto).

enforced in these crystals, because the residual stresses in microstructures are low regardless of lattice-parameter values.

© 2006 Elsevier Ltd. All rights reserved.

Keywords: Shape-memory alloys; CuZnAl; Long-period stacking; Compatibility; Microstructures

1. Introduction

Reversible martensitic transformations are at the basis of the advantageous properties exhibited by many smart crystalline materials, such as shape-memory alloys. A detailed understanding of the transition mechanisms, and the related phenomena of twinning and microstructure formation, is necessary for the control, improvement and design of new active substances (James and Hane, 2000; James and Zhang, 2005). Among memory alloys, the ones based on Cu, with a cubic austenite and a monoclinic martensite (such as CuZn, CuZnAl, CuAlNi, and several others, see for instance Table 5), are well known, and have enjoyed fairly broad investigation. Recent theoretical studies of these substances include Falk and Konopka (1990), Hane (1999), James and Hane (2000), Lexcellent et al. (2002), and Lexcellent and Blanc (2004). In this paper we further investigate the cubic-to-monoclinic transformation in these alloys, with a two-fold goal: firstly, to gain a better understanding of the mechanism producing faulted long-period stacking martensites in these metals, and, secondly, to analyze in more detail some typical microstructures associated with this phase transition, in particular the wedge configuration such as in Fig. 6.

Microscale transformation mechanism: The ordered alloys considered here exhibit, at higher temperature, a cubic bcc-based austenite, and, at lower temperature or under suitable loading, a (faulted) M9R or M18R monoclinic martensite (Fig. 2). We describe both phases in Section 2. Geometrically, when atomic species are disregarded, the M9R and M18R structures coincide; they are both slight deformations of the close-packed 9R structure (Strukturbericht C19). This martensitic transformation is thus a slightly distorted version of the bcc-to-9R transition, occurring in a number of elements, such as Li or Na (see the Appendix). Various literature indeed describes the cubic-to-monoclinic transition in Cu-based alloys as the ‘close-packing’ of a bcc lattice,¹ i.e., as a phase change taking the bcc structure to one composed by a stack of close-packed atomic planes. This will be the basic assumption in the present study.

As is well known, the compaction of a bcc lattice occurs through the two-step process (I)–(II) recalled in the Appendix, whereby the nets of rhombi on the densest $(110)_{\text{bcc}}$ planes become close-packed, and adjacent $(110)_{\text{bcc}}$ planes, once compacted, suitably slide on top of each other in a ‘zig-zag’ pattern so as to achieve the close-packing of the whole ensemble in three dimensions. The final stacking sequence then characterizes the structure, which, in principle, may be periodic as in the fcc, hcp, or 9R close-packed structures, or non-periodic.

¹For instance, Barrett and Massalski (1980, p. 531), mention that the transformation ‘from the bcc phase to close-packed phases’ occurs in several elements as well as in CuZn, CuAl, and other alloys; see also Gonzàles-Comas et al. (1997). For some literature treating close-packing transformations, see Overhauser (1984), Berliner et al. (1989), Schwarz and Blaschko (1990), Liu and Cohen (1991), Berliner et al. (1992), Ernst et al. (1992), Schwarz et al. (1992), Krystian and Pichl (2000), and Neaton and Ashcroft (2001).

From the two-step mechanism above we derive the ‘microscale’ deformation gradient (i.e., the matrix of the lattice distortion) which is at the root of all bcc-to-close-packed transformations. In the ideal case this coincides (up to a rigid-body rotation) with the classical Bain stretch related to the bcc-to-fcc transformation. The different close-packed configurations are then interpreted as the result of suitable piecewise-linear deformations involving at the microscale, in a layering pattern, the variants of the Bain stretch (combined with suitable rigid-body rotations).

As the bcc-to-M9R or bcc-to-M18R transformations of interest here do not take place in a perfect monoatomic bcc crystal, but, rather, in lattices where two or more kinds of atoms are present, these phase changes are, as mentioned, slightly distorted versions of a perfect bcc-to-compact transformation. For this reason, the relevant microscale stretches do not coincide with, but are close to, the Bain-stretch variants. In Section 3, we calculate such microstretches, where three small parameters are present, so that they have monoclinic symmetry.² We verify that in the case of the elemental crystals exhibiting the 9R structure, such small parameters are virtually zero, i.e., their microstrain coincides with the Bain stretch. The latter has three symmetry-related variants; in contrast, there are 12 variants in the non-ideal case of the near-Bain microstretch of memory alloys, which we make explicit in Section 4, see Fig. 4.

Mesoscale martensitic structures: The final sequence of close-packed planes characterizing the martensitic structure at the ‘mesoscale’ can be derived by using the microscale strain-variants in the compatibility equations for the austenite/martensite interface. This follows an adaptive-phase approach as in Lovey (1987), Khachatryan et al. (1991), Krystian and Pichl (2000). In Section 5, we determine all the transformation-twin systems originating from this mechanism, and in Section 6, we find the habit planes. The coherence calculations produce the long-period structure of the low symmetry phase, with the associated average strain matrix describing the mesoscale deformation of the martensite. Only one of the solutions to the corresponding equations turns out to be physically significant, giving correctly the stacking sequence of the observed long-period M9R–M18R structures and their habit planes. It also determines the density of the stacking faults that ever accompany the formation of the M9R–M18R martensite. Such deviations from the ideal M9R–M18R sequence arise as a necessary consequence of the austenite/martensite compatibility conditions.³

A version of the mesoscale M9R–M18R martensite strain was derived also by Lovey (1987), who assumed a tetragonal strain at the microlevel (see Section 6.4), and by Hane (1999), who derived the martensitic mesoscale deformation by considering the 6M1 martensitic cell (see Section 6.4). Our procedure, which takes into account both the monoclinicity of the microstrain and the stacking faults in the martensite, gives numerically small discrepancies with respect to such previous proposals. However, determining these quantities precisely is a relevant question because, as indicated by James and Zhang (2005), there is a potentially sensitive dependence of the material’s macroscopic

²This should not be confused with the fact that the ‘mesoscale’ long-period stacking martensite is also monoclinic. Compare with the similar, if less detailed, approach by Lovey (1987), who describes the approximate bcc-to-compact transition with a microscale tetragonal strain. See also Remark 3 in Section 4.

³Indeed, stacking faults are always present to alter the perfect stacking sequence ABCBCACAB... of the M9R–M18R structures, even in monoatomic 9R crystals (Gooding and Krumhansl (1988)). For this reason these are often referred to as ‘faulted’ martensites—see for instance Chakravorty and Wayman (1977), Redfield and Zangwill (1986), Lovey et al. (1987), Lovey (1987), Smith et al. (1990).

behavior (such as effective stress–strain relation, hysteresis, etc.) on the transformation-strain parameters.

Stressed wedge microstructure: We use the M9R–M18R mesoscale strain and its variants to analyze some typical microstructures observed in CuZnAl martensites. In particular, in Section 7, we investigate the thermally induced wedge observed in CuZn_{13,3}Al_{17,2}, as shown in Fig. 6 taken from Saburi and Wayman (1979).

The wedge is an important microstructure in shape-memory alloys, because it is recognized as a main favorable avenue for the martensitic transformation, allowing for easy nucleation and growth of the martensite into the austenite (see for instance Otsuka and Shimizu, 1974; Tan and Xu, 1990). The general question of kinematic compatibility for this morphology has therefore been studied in a number of works, for several materials and transformations (Bhattacharya, 1991; Hane and Shield, 1998; Hane and Shield, 1999a, b; James and Hane, 2000; Hane and Shield, 2000). A significant result of these studies is that the compatibility conditions for energy-minimizing microstructures, such as the wedge, may require special lattice-parameter relations to be satisfied, and that such relations indeed hold with good approximation in a number of memory alloys. This is linked to the origin, or the enhancement, of the phase transition reversibility and the memory effect in the material.

We find that the wedge morphology is not compatible in CuZnAl at zero stress. This is in agreement with the conclusions of James and Hane (2000), who indicate the wedge to be impossible in these alloys. In order to clarify CuZnAl wedge observations such as in Fig. 6, we revisit this question by estimating how far this microstructure is from being compatible, considering that stresses must be present so that compatibility be achieved. We introduce a natural non-compatibility indicator (Fig. 8) and verify, through a suitable finite-element procedure, that wedge stresses are indeed tolerable as they cause minimal plasticity-related damage in the crystal (Fig. 10). This contributes to clarify why such configuration is observed in CuZnAl in spite of its non-coherence at zero stress. We learn, furthermore, that wedge stresses are largely independent of composition, remaining low in the range of all the lattice parameters reported for these materials (Table 6 and Fig. 11).

Conclusions: Some general suggestions are derived from our study. Firstly, the martensitic microstructures that are observed even in rather good memory alloys are in general under at least moderate stress, involving lattice deformations that are measurably away from the bottom of the energy wells available to the material, the CuZnAl wedge being a case in point. The formation of stressed ensembles does not impair the reversibility of the phase change, as long as stresses are low and generate minimal damage in the lattice. We find, furthermore, that the stresses in the microstructure do not exhibit great sensitivity to lattice-parameter variations, remaining low in a wide range of compositions, with no need for tuning. The role of special lattice-parameter relations guaranteeing the existence of distinctive microstructures at stress-free conditions might thus not be as central as earlier conjectured. While the macroscopic behavior and desirable properties of a multiphase crystalline material might depend in a delicate way on its transition strain (or lattice) parameters, it appears that such sensitive dependence may not be the case for some memory alloys, such as CuZnAl.

2. Austenite and martensite

We consider Cu-based shape-memory alloys mostly focussing on the CuZnAl system, for which experimental data are most abundant (see the Appendix). Under suitable

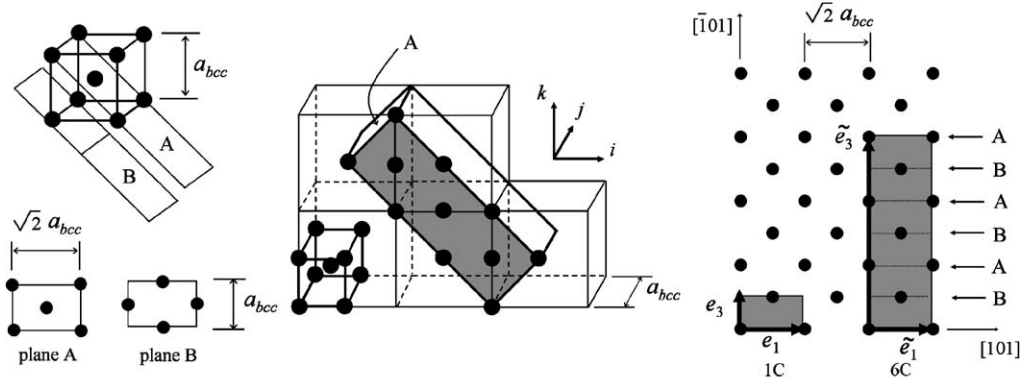


Fig. 1. The austenitic phase (whose structure is bcc ‘A2’ if the differences in species of the atoms are disregarded), and its cells 1C and 6C (shaded).

conditions of composition and quenching, these alloys assume metastable ordered configurations with *cubic* symmetry (austenite), and, for lower temperatures, with *monoclinic* symmetry (martensite). Except when otherwise noted, in what follows we consider these crystals as geometric structures whose points are all indistinguishable, disregarding the differences in atomic species (no ‘colors’ of the lattice points). All compositions are given in at%.

Cubic austenite: The cubic phase may have several configurations, distinguished by ordering. Through quenching, a disordered bcc (A2) phase is transformed into the ordered B2 structure, or, depending on composition, also into the L₂₁ or DO₃ structures—see [Strukturbericht \(1928–1932\)](#) for nomenclature. The austenitic B2, DO₃, and L₂₁ structures are all ‘bcc-based’, and they all coincide, in our no-color approximation, with a bcc Bravais lattice, with parameter a_{bcc} and whose three mutually orthogonal four-fold axes define an orthonormal basis $\{i, j, k\}$ and the associated standard bcc Miller indices. Unless otherwise noted, we give the matrix expressions of all tensors with respect to this basis.⁴ For later purposes, it is useful to consider the vectors $e_1 = a_{\text{bcc}}(i + k)$, $e_2 = a_{\text{bcc}}j$, $e_3 = (a_{\text{bcc}}/2)(k - i)$, spanning the ‘1C cell’ shown in Fig. 1, which contains one atom of the bcc lattice. Correspondingly, the ‘6C cell’ is spanned in the austenite by the vectors $\tilde{e}_1 = e_1$, $\tilde{e}_2 = e_2$, $\tilde{e}_3 = 6e_3$, in the same figure. The point group \mathcal{P} of the austenite is (for brevity we only list the rotations):

$$\mathcal{P} = \{1, R_i^\pi, R_j^\pi, R_k^\pi, R_i^{\pi/2}, R_i^{3\pi/2}, R_j^{3\pi/2}, R_j^{\pi/2}, R_k^{\pi/2}, R_k^{3\pi/2}, R_{i+k}^\pi, R_{i-k}^\pi, R_{i+j}^\pi, R_{i-j}^\pi, R_{j+k}^\pi, R_{j-k}^\pi, R_{i+j+k}^{2\pi/3}, R_{i+j-k}^{2\pi/3}, R_{i-j+k}^{2\pi/3}, R_{i-j-k}^{2\pi/3}, R_{i+j+k}^{4\pi/3}, R_{i+j-k}^{4\pi/3}, R_{i-j+k}^{4\pi/3}, R_{i-j-k}^{4\pi/3}\}, \quad (2.1)$$

where R_n^θ denotes the rotation through an angle θ about the axis n .

Monoclinic martensite: From the above B2, DO₃, or L₂₁ austenite, a martensitic transformation in CuZnAl is induced by lowering the temperature, or by applying suitable

⁴This coincides with any of the A2, B2, DO₃, or L₂₁ indexations used in the literature. However, the lattice parameters for the DO₃ or L₂₁ structures, which are referred to cubic cells that have twice the cubic-side length of A2 or B2, must be accordingly adjusted: $a_{\text{DO}_3} = 2a_{\text{B2}} = 2a_{\text{bcc}}$. Table 5 gives a summary of lattice-parameter values reported in the literature.

mechanical loading. The martensite is monoclinic, and is usually described by the M18R cell when the austenite is DO_3 or $L2_1$, or by the M9R cell for the B2 austenite (Fig. 2). These structures coincide in our no-color approximation. Two other cells, called 6M1 and 6M2, have also been used to describe this monoclinic martensite. It is useful to put in evidence in this phase also the ‘1M cell’; all cells are shown in Fig. 2. (We denote the 1C, 6C and 1M cells following the lead of Otsuka et al. (1993); we notice the 1M cell is implicitly considered also in the computations by Gui et al. (1988).) Indexing in the martensite is usually done with respect to the M18R or the M9R cells, whose lattice parameters a , b , c , and θ are shown in Fig. 2.

Remark 1. In the literature on shape-memory alloys exhibiting long-period stacking structures, the martensite is called 18R or M18R (i.e., ‘modified’ 18R) depending on whether the angle θ in Fig. 2 is 90° or not; similarly for the 9R case. Such 9R and 18R structures always have monoclinic symmetry (so that they are not orthorhombic even when θ in the M9R–M18R cell is 90°). However, in the literature unrelated to such materials, the symbol ‘9R’ only indicates the C19 structure in the no-color case, which has rhombohedral symmetry (see for instance Liu and Cohen, 1991; Blaschko et al., 1999), and which becomes, through a small deformation, the ‘monoclinic 9R’ structure presently considered. To avoid confusion, for the latter we only use the symbols M9R or M18R. Notice that as for the hcp case, also in the 9R structure special parameters are needed in order that 9R be *close-packed*, as is observed, to great approximation, in a number of elemental crystals (see for instance Table 5).

Lattice-parameter definitions: For the austenitic cells one has $a_{DO_3} = 2a_{B2} =: 2a_{bcc}$. For the martensitic cells in Fig. 2, one has $a_{1M} = a_{6M1} = a_{M18R} = a_{M9R}$, and $b_{1M} = b_{6M1} = b_{6M2} = b_{M9R} = b_{M18R}/2$. As the stacked atomic planes in the M18R cell are twice as many

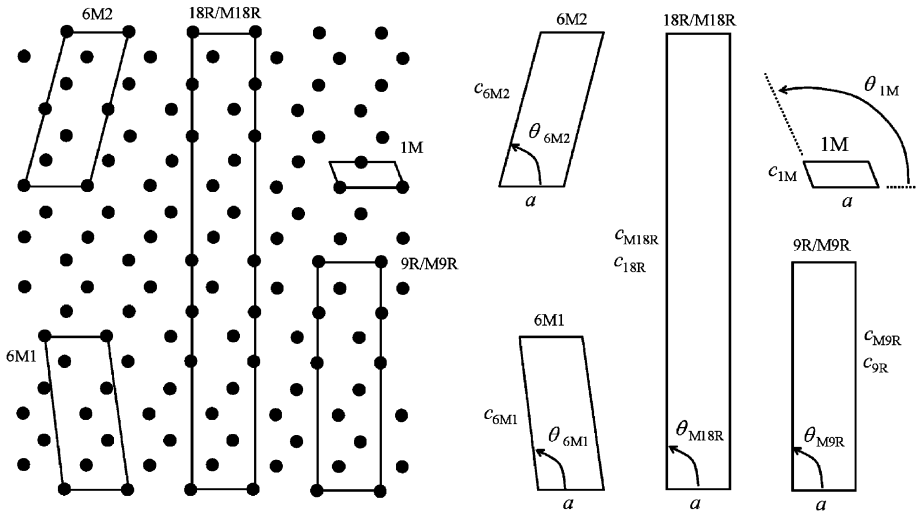


Fig. 2. Section of the martensitic structure (atomic species are disregarded) and the lattice parameters of various cells. The parameter b (not shown) measures the dimension of the cell in the direction orthogonal to the page, and is the same for all cells. Also the parameter a is the same for all cells.

as in the M9R cell, one also has $c_{M18R} = 2c_{M9R}$, while $\theta_{M18R} = \theta_{M9R}$. Some trigonometry gives the other parameters of the cells 6M1 and 1M in terms of the parameters of the M18R or M9R cells; the corresponding formulas (A.1) and (A.2) are given explicitly in Appendix A.2. Table 5 summarizes the known lattice-parameter data for a number of materials.

3. The cubic-to-monoclinic transformation mechanism in Cu-based alloys

3.1. The 6C \leftrightarrow 6M1 mechanism

Hane (1999) indicates the correspondence between the austenitic cell 6C and the martensitic cell 6M1 (together with a suitable shuffling of the atoms inside such non-unit cells, see Fig. 3) to be the basic mechanism for the phase transformation in these alloys (see also Section 6.4). The (symmetric, positive-definite) stretch matrix characterizing this lattice distortion is obtained by considering the displacements of the corner atoms of the cells in the 6C \leftrightarrow 6M1 mechanism. For instance, for the alloy CuZn₁₅Al₁₇, the lattice-parameter data in Table 5 give the following transformation stretch:

$$U_{6M1} = \begin{pmatrix} 1.0095 & 0 & 0.0253 \\ 0 & 0.9093 & 0 \\ 0.0253 & 0 & 1.0862 \end{pmatrix}, \quad (3.1)$$

whose eigenvalues are 0.9093, 1.0019, 1.0938. Here and in the following, we use CuZn₁₅Al₁₇ for our numerical examples because the lattice parameters of the alloy CuZn_{13,3}Al_{17,2} exhibiting the wedge in Fig. 6 are not available. In Saburi and Wayman (1979), from which the figure is taken, the authors refer to the lattice parameters of CuZn₁₅Al₁₇ in place of the unknown ones of CuZn_{13,3}Al_{17,2}.

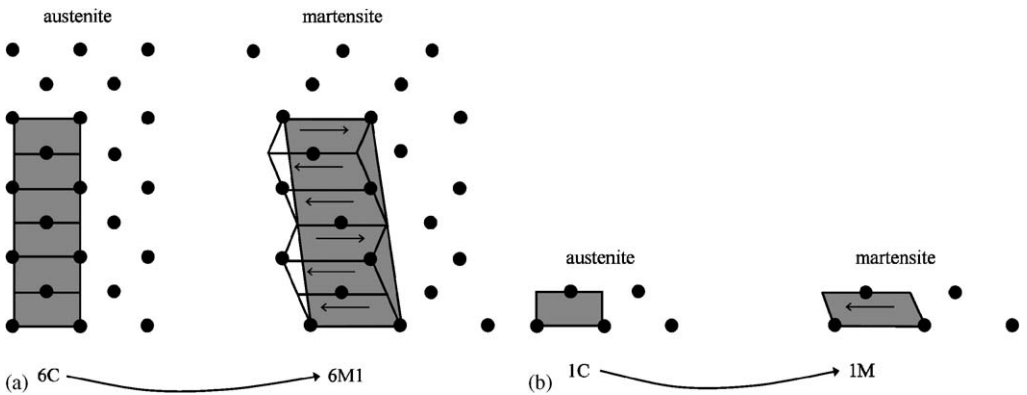


Fig. 3. (a) Schematic representation of the 6C \leftrightarrow 6M1 transformation mechanism, which puts the austenitic cell 6C in correspondence with the martensitic cell 6M1. (b) The 1C \leftrightarrow 1M correspondence, which gives the basic close-packing mechanism (see Section 3.2). The 6C \leftrightarrow 6M1 and 1C \leftrightarrow 1M correspondences produce the stretch matrices in (3.1) and (3.2)–(3.5), respectively. The arrows in the 6M1 cell refer to the 1M-twinning mechanism described in Section 6.2.

3.2. The elementary 1C ↔ 1M mechanism and the Bain stretch

As mentioned in the Introduction, a more basic viewpoint on the bcc-to-M9R (or the bcc-to-M18R) transformation takes into account the fact that, geometrically, the archetype for the latter is the well-known bcc-to-9R phase change. This is in turn a special case of a bcc-to-close-packed transition. Some main facts about this are mentioned in the Appendix, in particular, we recall the basic compaction mechanism described by steps (I)–(II) in Appendix A.1. In terms of the austenitic and martensitic cells considered in Section 2, steps (I)–(II) correspond to the 1C ↔ 1M transformation, schematized in Fig. 3. This only concerns the close-packing of two nearby planes, so that a way to select the stacking sequence producing the final structure is also needed, which we discuss in Sections 6.2 and 6.3. We first obtain the stretch matrix that characterizes the 1C ↔ 1M lattice distortion: in the ideal case of two adjacent perfectly close-packed planes, this is calculated to be

$$U_{1M}^{\text{ideal}} = d \begin{pmatrix} 2^{-1/6} & 0 & 0 \\ 0 & 2^{-1/6} & 0 \\ 0 & 0 & 2^{1/3} \end{pmatrix} = dU_{\text{Bain}}, \quad (3.2)$$

where d is a scale parameter and U_{Bain} is the well-known (isochoric) Bain stretch, i.e., the stretch responsible for the bcc-to-fcc transformation.

In the (non-ideal) case of our alloys, the stretch matrix U_{1M} derived from the 1C ↔ 1M correspondence does not coincide with the Bain stretch U_{1M}^{ideal} in (3.2), but is close to it. To write such U_{1M} , we first obtain the lattice parameters of the 1M cell in the martensite through formulas (A.2). From these, the entries of U_{1M} can be calculated obtaining

$$U_{1M} = \begin{pmatrix} \rho_{1M} & 0 & \sigma_{1M} \\ 0 & \beta_{1M} & 0 \\ \sigma_{1M} & 0 & \tau_{1M} \end{pmatrix} \approx (\det U_{1M})U_{\text{Bain}}. \quad (3.3)$$

The values of β_{1M} , ρ_{1M} , σ_{1M} and τ_{1M} are given explicitly in terms of the 1M lattice parameters by formulas (A.3)–(A.4) in the Appendix.

The form above of U_{1M} in (3.3) shows that the 1M cell in the martensite is monoclinic (Pitteri and Zanzotto, 2002). We have in (3.3) that $U_{1M} \approx (\det U_{1M})U_{\text{Bain}}$ because, for our materials, there appear in U_{1M} three small parameters distinguishing it from the ideal bcc-to-fcc Bain stretch in (3.2), that is,

$$\sigma_{1M} \approx 0, \quad \rho_{1M} - \beta_{1M} \approx 0, \quad (\tau_{1M}/\beta_{1M}) - \sqrt{2} \approx 0. \quad (3.4)$$

This can be compared to Lovey (1987), who only introduces one small parameter in his analysis of M9R–M18R martensites, i.e., the ‘tetragonality’ ψ of the fcc-like cell obtained from the 1C ↔ 1M close-packing mechanism.⁵

As an example, we calculate U_{1M} in (3.3) for the same alloy $\text{CuZn}_{15}\text{Al}_{17}$ considered in (3.1). From the lattice parameters in Table 5 and the formulas above, we obtain the

⁵In detail, Lovey (1987) assumes $\beta_{1M} = \rho_{1M}$ and $\sigma_{1M} = 0$ in our notation, so that his small tetragonality parameter is $\psi := (\tau_{1M}/\beta_{1M}) - \sqrt{2} \approx 0$. From (3.3), we see that the 1C cell has actually monoclinic, rather than tetragonal (or orthorhombic) shape, as the experimental lattice-parameter data give, for instance, σ_{1M} small but not zero (although the corresponding error possibly includes the case $\sigma_{1M} = 0$ for some alloys).

following stretch matrix:

$$U_{1M} = \begin{pmatrix} 0.9388 & 0 & 0.0146 \\ 0 & 0.9093 & 0 \\ 0.0146 & 0 & 1.1675 \end{pmatrix} \approx 0.9964 U_{\text{Bain}}, \quad (3.5)$$

which, as previously discussed, is an almost isochoric monoclinic stretch that is close to U_{1M}^{ideal} in (3.2) for $d = 0.9964$. For lithium, the corresponding stretch U_{1M} , calculated from the lattice parameters by [Berliner et al. \(1989\)](#), is virtually indistinguishable from U_{1M}^{ideal} in (3.2) for $d = 1.0009$, i.e., from the isochoric Bain stretch:

$$U_{1M} = \begin{pmatrix} 0.8909 & 0 & 0.0005 \\ 0 & 0.8915 & 0 \\ 0.0005 & 0 & 1.2603 \end{pmatrix}. \quad (3.6)$$

4. Variants

To analyze the martensitic microstructure we need the symmetry-related variants U_i of the transformation stretch matrix U (be it U_{Bain} , U_{1M} , or U_{6M1}), which are given by the distinct stretches among those of the form:

$$U_i = R_i^T U R_i, \quad (4.1)$$

where R_i is any rotation in the point group (2.1) of the austenite.

Variants of the Bain stretch: For $U = U_{\text{Bain}} =: B_3$ as in (3.2), definition (4.1) gives the three variants ([Fig. 4](#)):

$$B_1 = \begin{pmatrix} 2^{1/3} & 0 & 0 \\ 0 & 2^{-1/6} & 0 \\ 0 & 0 & 2^{-1/6} \end{pmatrix}, \quad B_2 = \begin{pmatrix} 2^{-1/6} & 0 & 0 \\ 0 & 2^{1/3} & 0 \\ 0 & 0 & 2^{-1/6} \end{pmatrix},$$

$$B_3 = \begin{pmatrix} 2^{-1/6} & 0 & 0 \\ 0 & 2^{-1/6} & 0 \\ 0 & 0 & 2^{1/3} \end{pmatrix}. \quad (4.2)$$

Variants of the monoclinic stretch U_{1M} : For $U = U_{1M}$ in (3.3), definition (4.1) gives the following twelve distinct matrices ([Pitteri and Zanzotto, 2002](#)):

$$U_1 = \begin{pmatrix} \beta & 0 & 0 \\ 0 & \rho & \sigma \\ 0 & \sigma & \tau \end{pmatrix}, \quad U_2 = \begin{pmatrix} \beta & 0 & 0 \\ 0 & \rho & -\sigma \\ 0 & -\sigma & \tau \end{pmatrix}, \quad U_3 = \begin{pmatrix} \beta & 0 & 0 \\ 0 & \tau & \sigma \\ 0 & \sigma & \rho \end{pmatrix},$$

$$U_4 = \begin{pmatrix} \beta & 0 & 0 \\ 0 & \tau & -\sigma \\ 0 & -\sigma & \rho \end{pmatrix}, \quad U_5 = \begin{pmatrix} \tau & 0 & \sigma \\ 0 & \beta & 0 \\ \sigma & 0 & \rho \end{pmatrix}, \quad U_6 = \begin{pmatrix} \tau & 0 & -\sigma \\ 0 & \beta & 0 \\ -\sigma & 0 & \rho \end{pmatrix},$$

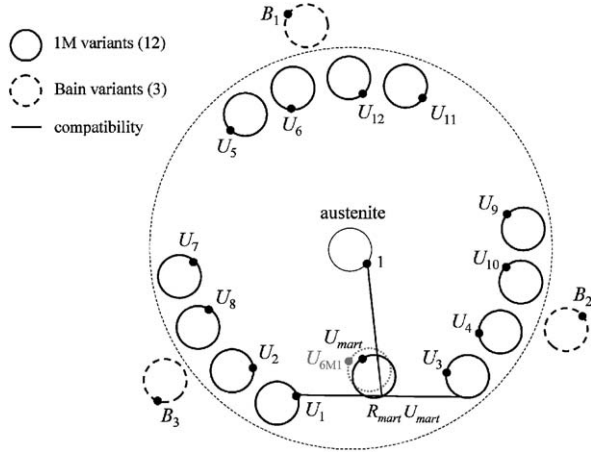


Fig. 4. Schematic representation of the 12 monoclinic variants U_i , $i = 1, \dots, 12$, that exist, for the microscale stretch U_{1M} , in nine-dimensional strain space (see (4.3)). Each circle represents U_i together with its orbit RU_i under the set of all rigid-body rotations. Analogously for the three variants B_r , $r = 1, 2, 3$, of the isochoric Bain stretch in (4.2), and for the identity tensor 1, which corresponds to the reference austenitic configuration. The monoclinic variants U_i are close, in clusters of four, to each one of the three Bain variants B_r . Some ‘rank-1 connections’ as in (5.1) between kinematically compatible stretches U_i are indicated by straight lines. The mesoscale martensitic stretch U_{mart} so originated (see formula (6.5)) is also shown, together with the nearby stretch U_{6M1} of Section 3.1. Both U_{mart} and U_{6M1} have 12 variants (omitted for clarity). A suitable Ericksen–Pitteri neighborhood of 1 (represented by the large dashed circle) contains all such monoclinic variants, but not the stretches B_r (see Remark 3).

$$\begin{aligned}
 U_7 &= \begin{pmatrix} \rho & 0 & \sigma \\ 0 & \beta & 0 \\ \sigma & 0 & \tau \end{pmatrix}, & U_8 &= \begin{pmatrix} \rho & 0 & -\sigma \\ 0 & \beta & 0 \\ -\sigma & 0 & \tau \end{pmatrix}, & U_9 &= \begin{pmatrix} \rho & \sigma & 0 \\ \sigma & \tau & 0 \\ 0 & 0 & \beta \end{pmatrix}, \\
 U_{10} &= \begin{pmatrix} \rho & -\sigma & 0 \\ -\sigma & \tau & 0 \\ 0 & 0 & \beta \end{pmatrix}, & U_{11} &= \begin{pmatrix} \tau & \sigma & 0 \\ \sigma & \rho & 0 \\ 0 & 0 & \beta \end{pmatrix}, & U_{12} &= \begin{pmatrix} \tau & -\sigma & 0 \\ -\sigma & \rho & 0 \\ 0 & 0 & \beta \end{pmatrix}.
 \end{aligned} \quad (4.3)$$

We notice that given any two variants U_i and U_j in (4.3), there are two elements R in the austenitic point group (2.1) relating U_i and U_j as in (4.1). For all i and j , this information, which is useful for classifying twinning modes, can be summarized in a table analogous to the one given in Hane and Shield (1999b); for brevity we do not report this explicitly here.

Remark 2. The monoclinic variants in (4.3) produce 12 configurations which, in sets of four (see each row of the list in (4.3)), share a monoclinic axis originating from one of the three four-fold axes along the edges of the bcc austenitic cell, see Pitteri and Zanzotto (1998) or (2002) for details. With the lattice parameters of our materials, these 12 variants are close, in suitable sets of four which are reported in Fig. 4, to each one of the three Bain matrices B_r in (4.2). Also the variants of the stretch U_{6M1} in (3.1) are of the same monoclinic type as U_{1M} ; consequently their list formally coincides with the list (4.3).

Remark 3. The configurations reached through the ideal Bain stretches B_r in (4.2) are at the boundary of a maximal ‘Ericksen–Pitteri neighborhood’ (Ericksen, 1980; Pitteri, 1984; Ball and James, 1992) of the parent bcc phase. For this reason, as discussed in Bhattacharya et al. (2004), reconstructive martensitic transformations such as bcc-to-fcc, or bcc-to-9R, are irreversible. On the contrary, the monoclinic stretch U_{1M} and its variants (4.3) give configurations within such a neighborhood of the bcc austenite. This is an important factor giving the martensitic transformation in our alloys the potential of being reversible, and to display the memory effect.

5. Twinning

In this section, we briefly analyze the transformation twins arising in the cubic-to-monoclinic phase change in our materials. The related equations are discussed for instance in Wechsler et al. (1953), Wayman (1977), Ericksen (1980, 1985), Ball and James (1987, 1992), James and Hane (2000), Pitteri and Zanzotto (2002), and Bhattacharya (2003).

5.1. Kinematic compatibility conditions and transformation twins

Let an austenitic single crystal (reference configuration) change to the martensitic phase described by the variant stretches U_1, \dots, U_n (for instance, the variants listed in (4.3)). Transformation twinning is then described, up to inessential rigid-body rotations, by pairwise homogeneous deformations with gradients RU_j and U_i (for given i, j between 1 and n) on the two sides of a plane with unit normal \hat{n} , such that the deformation is continuous across that plane. This holds if the following ‘twinning equation’, which derives from the Hadamard compatibility conditions, is satisfied:

$$RU_j - U_i = a \otimes \hat{n} \quad (5.1)$$

(in this case RU_j and U_i are said to be ‘rank-1 connected’). Here the unknowns are the ‘twinning rotation’ R , the ‘shear vector’ a , and the unit normal \hat{n} to the twin interface in the reference configuration. The vector $m = U_i^{-T} \hat{n}$ gives the normal to the plane in the deformed configuration, on which the deformation gradient is discontinuous, and the ‘twinning shear’ is defined by $S := 1 + a \otimes U_i^{-1} \hat{n}$. The ‘twin elements’ utilized to describe twinning modes in the experimental literature are as follows: K_1 is the twin interface in the deformed configuration, that is, the invariant plane of the shear S ; η_1 is the shear direction (the direction of a); K_2 is the ‘second undistorted plane’ of the shear S ; and η_2 is the intersection of K_2 with the ‘plane of shear’ given by $U_i^{-1} \hat{n}$ and a (see for instance Barrett and Massalski, 1980).

A necessary and sufficient condition guaranteeing that there are solutions (a, \hat{n}) to (5.1) is that the matrix $C := (U_j U_i^{-1})^T (U_j U_i^{-1})$ has (positive) eigenvalues $\mu_1 \leq \mu_2 \leq \mu_3$, such that

$$\mu_2 = 1. \quad (5.2)$$

Such solutions, when they exist, come in pairs describing two ‘conjugate twins’; they are given explicitly by formula (A.5) in the Appendix. It is known that when the two martensitic stretches U_i and U_j in (5.1) are related as in (4.1) through at least one operation R that is a 180° -rotation, these solutions to the compatibility (5.1) always exist, and have explicit expressions detailed for instance by Gurtin (1983). They describe the classical ‘type-I’ and ‘type-II’ conjugate twins, whose twinning operations are

180°-rotations about the axis m or a , respectively. When U_i and U_j are related through (4.1) by *two* different 180°-rotations, such solutions correspond to two ‘compound twins’ (which are twins at once of type I and II); see for instance [Pitteri and Zanzotto \(2002\)](#). As usual, we refer to type-I, -II, and compound twins, as ‘conventional’.

5.2. Transformation twins for the monoclinic variants in (4.3)

We can now analyze explicitly the twins in a cubic-to-monoclinic transformation with variant stretches coming from the list in (4.3). We indicate by $(i;j)$ a pair of stretches U_i and U_j , symmetry-related as in (4.1), and such that Eq. (5.1) has solutions. Following [Hane and Shield \(1999b\)](#), it is convenient to group the couples $(i;j)$ into sets according to the criterion that $(k:l)$ and $(i;j)$ are equivalent when they are related by a rotation Q in the cubic group (2.1) as follows:

$$U_k = Q^T U_i Q \quad \text{and} \quad U_l = Q^T U_j Q. \tag{5.3}$$

The twinning solutions for the pair $(k:l)$ can thus be deduced from the solution for the pair $(i;j)$, by setting, in obvious notation: $\hat{n}_{kl} = Q^T \hat{n}_{ij}$, $a_{kl} = Q^T a_{ij}$ and $R_{kl} = Q^T R_{ij} Q$.

By using this criterion, we find *seven* distinct transformation twinning modes, whose main features, derived from Eqs. (A.5) in the Appendix, are summarized in [Table 1](#).

First set of compound twins $S'_c = \{(1:2) (3:4) (5:6) (7:8) (9:10) (11:12)\}$;

Second set of compound twins $S''_c = \{(1:3) (2:4) (5:7) (6:8) (9:11) (10:12)\}$;

First set of type-I and -II twins $S'_t = \left\{ \begin{array}{l} (1:7) (1:8) (2:7) (2:8) (3:9) (3:10) \\ (4:9) (4:10) (5:11) (5:12) (6:11) (6:12) \end{array} \right\}$;

Second set of type-I and -II twins $S''_t = \left\{ \begin{array}{l} (1:11) (1:12) (3:5) (3:6) (4:5) (4:6) \\ (7:9) (7:10) (8:9) (8:10) (2:11) (2:12) \end{array} \right\}$;

Set of generic non-conventional twins $S_{\text{gnc}} = \{(1:4) (2:3) (5:8) (6:7) (9:12) (10:11)\}$;

First set of non-generic twins $S'_{\text{ng}} = \left\{ \begin{array}{l} (1:5) (1:6) (2:5) (2:6) (3:11) (3:12) \\ (4:11) (4:12) (5:9) (5:10) (6:9) (6:10) \\ (7:3) (7:4) (8:3) (8:4) (9:1) (9:2) \\ (10:1) (10:2) (11:7) (11:8) (12:7) (12:8) \end{array} \right\}$;

Second set of non-generic twins $S''_{\text{ng}} = \left\{ \begin{array}{l} (5:1) (6:1) (5:2) (6:2) (11:3) (12:3) \\ (11:4) (12:4) (9:5) (10:5) (9:6) (10:6) \\ (3:7) (4:7) (3:8) (4:8) (1:9) (2:9) \\ (1:10) (2:10) (7:11) (8:11) (7:12) (8:12) \end{array} \right\}$.

Table 1

Main features of the seven twin systems originating from the monoclinic variants in (4.3)

Set of twins	Genericity	Type	Indices in the cubic austenite			
			K_1	η_1	K_2	η_2
S'_c	Generic	Compound	(0 0 1)	[0 $\bar{1}$ 0]	(0 1 0)	[0 0 $\bar{1}$]
		Compound	(0 1 0)	[0 0 $\bar{1}$]	(0 0 1)	[0 $\bar{1}$ 0]
S''_c	Generic	Compound	(0 $\bar{1}$ 1)	[0 $\bar{1}$ $\bar{1}$]	(0 1 1)	[0 1 $\bar{1}$]
		Compound	(0 1 1)	[0 $\bar{1}$ 1]	(0 $\bar{1}$ 1)	[0 1 1]
S'_t	Generic	Type-I	(1 $\bar{1}$ 0)	Irrat.	Irrat.	[$\bar{1}$ 1 0]
		Type-II	Irrat.	[$\bar{1}$ 1 0]	(1 $\bar{1}$ 0)	Irrat.
S''_t	Generic	Type-I	(1 0 $\bar{1}$)	Irrat.	Irrat.	[$\bar{1}$ 0 1]
		Type-II	Irrat.	[$\bar{1}$ 0 1]	(1 0 $\bar{1}$)	Irrat.
S_{gnc}	Generic	Non-conventional	Irrat.	Irrat.	Irrat.	Irrat.
		Non-conventional	Irrat.	Irrat.	Irrat.	Irrat.
S'_{ng}	Non-generic	Non-conventional	Irrat.	Irrat.	Irrat.	Irrat.
		Non-conventional	Irrat.	Irrat.	Irrat.	Irrat.
S''_{ng}	Non-generic	Non-conventional	Irrat.	Irrat.	Irrat.	Irrat.
		Non-conventional	Irrat.	Irrat.	Irrat.	Irrat.

The couple of variants (1: j) is considered in each twin family.

6. Austenite/martensite compatibility and resulting martensitic structures

To calculate the possible habit planes arising from the stretches in (4.3), we use the conditions for kinematic compatibility between the austenite and the twinned 1M martensite.

6.1. Habit-plane equations from the 1C \leftrightarrow 1M mechanism, and mesoscale stretch in the martensite

As the stretch U_{1M} does not satisfy (5.2), the austenite and a single variant of the 1M martensite cannot have a coherent interface. Then, typically, the phases assume the geometry of the austenite/twinned-martensite habit plane, schematically represented in Fig. 5. This involves the homogeneous austenite, a twinned (i : j) 1M-martensitic pair, and a transition layer. The compatibility conditions for this microstructure are given by the following equations (see Wechsler et al., 1953; Bowles, 1954; Wayman, 1977; Ball and James, 1987; Pitteri and Zanzotto, 2002; Bhattacharya, 2003):

$$RU_j - U_i = a \otimes \hat{n} \quad \text{and} \quad \bar{R}[\lambda RU_j + (1 - \lambda)U_i] - 1 = b \otimes \hat{m}, \quad (6.1)$$

where U_i and U_j are 1M-martensitic variants as in (4.3), λ is the volume fraction of the variant j in the (i : j)-twin layering, and a , \hat{n} , b , \hat{m} are suitable vectors (with \hat{n} and \hat{m} of unit norm; see Fig. 5). Necessary and sufficient conditions for the existence of solutions of (6.1) are given by Ball and James (1987). When such conditions hold, there exist two values λ_1 and λ_2 of the volume fraction λ that solve (6.1):

$$\lambda_1 = \frac{1}{2} \left(1 - \sqrt{1 + \frac{2}{\delta}} \right), \quad \lambda_2 = 1 - \lambda_1, \quad \delta = a \cdot U_i (U_i^2 - 1)^{-1} \hat{n}. \quad (6.2)$$

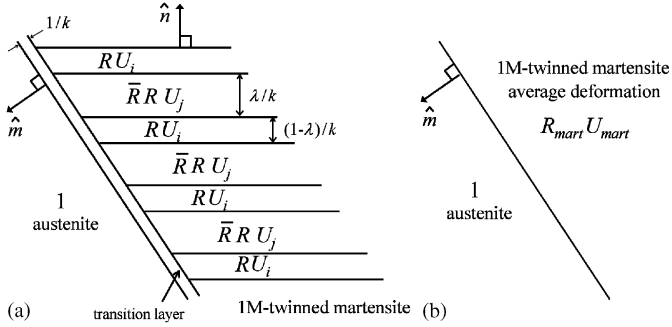


Fig. 5. Austenite/twinned-martensite layer interface. The deformation gradients are indicated in the left panel (a), while the right panel (b) shows the average (mesoscale) deformations as in (6.3).

Correspondingly, the habit-plane equation (6.1)₂ has two solutions for each value of λ . Therefore, for a given couple $(i;j)$, the system (6.1) for the habit plane has in general eight distinct solutions (four solutions if $\lambda_1 = \lambda_2 = 0.5$). Each such solution gives a stretch tensor, say U_{mart} , originating from the polar decomposition of the tensor $[\lambda R U_j + (1 - \lambda) U_i]$ in (6.1). Together with a suitable rotation R_{mart} , U_{mart} thus satisfies the following ‘average compatibility equation’ (which is but another way of writing (6.1)₂):

$$R_{\text{mart}} U_{\text{mart}} - 1 = b \otimes \hat{m}, \quad (6.3)$$

therefore U_{mart} measures the average (mesoscale) deformation in the 1M-twinned martensite near the interface with the austenite. Clearly, the entries of U_{mart} depend, through the polar decomposition of the tensor in (6.1)₂, on the austenitic and martensitic lattice parameters, i.e., on the entries $\beta_{1M}, \rho_{1M}, \sigma_{1M}, \tau_{1M}$ of U_{1M} in (3.3). Notice that, by (6.3), U_{mart} always has the middle eigenvalue equal to 1, as prescribed by (5.2).

6.2. Adaptive M18–M9R faulted martensite

We have analyzed the solutions of the habit-plane equations (6.1) for all the five 1M-twin families that are generic in Section 5.2, i.e., $S'_c, S''_c, S'_t, S''_t, S_{\text{gnc}}$. We find that

- No solutions exist for the twin systems S'_c and S'_t , while habit planes are possible for the twin systems S''_c, S''_t , and S_{gnc} .
- The two latter families, however, give physically unfavorable solutions, because system S''_t has 1M-twin interfaces that either have high indices (for the type-I twins) or are irrational (for the type-II twins), while twin system S_{gnc} gives solutions whose interfaces are all irrational. This makes these twins unlikely for fine layering at a habit plane.

Only the solutions originating from twin system S''_c appear to be relevant in the discussion of the habit planes, and of the corresponding long-period martensites, in our materials. From now on we concentrate on this case. The average stretch tensor U_{mart} in (6.3) is computed by layering with twins in the family S''_c , for instance by means of the 1M variants U_1 and U_3 in (4.3). In this case, Eq. (6.1)₁ gives two conjugate compound twins whose elements are all indicated in Table 1. Through each one of these solutions, one

obtains, from (6.2), the two values λ_1 and $\lambda_2 = 1 - \lambda_1$ which can be used in (6.1)₂ to find the corresponding habit planes and average martensitic stretches.

We first examine one of these twins, with elements $K_1(0 \bar{1} 1)$, $\eta_1[0 \bar{1} \bar{1}]$, $K_2(0 1 1)$, $\eta_2[0 1 \bar{1}]$ (see Table 1). In this case, the general expression (6.2) becomes

$$\lambda_1 = \frac{1}{2} \left(1 + \frac{\sqrt{\alpha_{1M}^2 - 1} \sqrt{\gamma_{1M}^2 \sin^2 \theta_{1M} - 1}}{\gamma_{1M} \cos \theta_{1M}} \right), \quad \lambda_2 = 1 - \lambda_1, \quad (6.4)$$

where $\alpha_{1M} > 1$, $\gamma_{1M} > 1$, and $\theta_{1M} > 90^\circ$, are as in (A.4). For values of the U_{1M} stretch parameters close to those pertaining to the materials in Table 5, we obtain for this (1:3)-twin volume fractions which are very close to $\frac{1}{3}$ or $\frac{2}{3}$ (see Table 6). This produces, if 1M-twinning occurs at the atomic scale, the M9R–M18R structure (whose angle θ_{M18R} is, in general, close to, but different from, 90°), as shown in Fig. 3(a), plus suitable stacking faults, discussed in Section 6.3. The corresponding average stretch has the following monoclinic form:

$$U_{\text{mart}} = \begin{pmatrix} \rho_{\text{mart}} & 0 & \sigma_{\text{mart}} \\ 0 & \beta_{\text{mart}} & 0 \\ \sigma_{\text{mart}} & 0 & \tau_{\text{mart}} \end{pmatrix}, \quad (6.5)$$

where $\rho_{\text{mart}}, \sigma_{\text{mart}}, \beta_{\text{mart}}, \tau_{\text{mart}}$ are suitable functions of the lattice parameters of the two crystal phases.

For instance, for $\text{CuZn}_{15}\text{Al}_{17}$, one calculates, from (6.4) and (6.3),

$$\lambda_1 = 0.3225, \quad U_{\text{mart}} = \begin{pmatrix} 1.0071 & 0 & 0.0252 \\ 0 & 0.9093 & 0 \\ 0.0252 & 0 & 1.0887 \end{pmatrix} \quad (6.6)$$

with eigenvalues: 0.9093, 1, 1.0959.

When the second value $\lambda_2 = 1 - \lambda_1$ of the volume fraction for the (1:3)-twin is used, we obtain habit planes that are equivalent to those found above through λ_1 . Correspondingly, the mesoscale stretch derived from λ_2 is a variant of the stretch U_{mart} found in (6.5). Since U_{mart} is of the same monoclinic type as U_{1M} and U_{6M1} (see Eqs. (3.1) and (6.6)), it has exactly the same 12 variants listed in (4.3). We retrieve these 12 variants (and the corresponding habit planes, which are all also crystallographically equivalent), by considering all the 1M-variant pairs (equivalent to (1:3)) belonging to set S_c'' of Section 5.2. This is summarized in Table 2.

For tensors as in (6.5), the expressions for the vectors a and \hat{m} in (6.3), which give explicitly the habit-plane normal in the reference configuration, are like the analogous ones written by Hane (1999) for U_{6M1} . They are readily derived from (A.5), and are not recalled here. For the alloy $\text{CuZn}_{15}\text{Al}_{17}$ as in (6.6), one obtains the habit plane $\hat{m}^+ = (-0.6804, 0.1999, 0.7050)_{\text{bcc}}$, which differs less than 5° from the habit plane for a Zn-rich CuZnAl alloy, experimentally reported by Takezawa et al. (1976) to be close to $\{21112\}_{\text{bcc}}$. For $\text{CuAl}_{14}\text{Ni}_4$ one finds a habit plane that is $\hat{m}^+ = (-0.6573, 0.1530, 0.7380)_{\text{bcc}}$, differing about 3° from the experimental report (551) by Otsuka et al. (1976). For Li, the calculated habit plane $\hat{m}^+ = (-0.6637, 0.1828, 0.7263)_{\text{bcc}}$ is also

Table 2

The average martensitic stretches obtained through the 1M-twins in family S_c'' of Section 5 give the 12 symmetry-related variants of U_{mart} as in list (4.3)

1M-twin in family S_c''	U_{mart} for λ_1	U_{mart} for $\lambda_2 = 1 - \lambda_1$	1M-twin in family S_c''	U_{mart} for λ_1	U_{mart} for $\lambda_2 = 1 - \lambda_1$
(1:3)	$U_{\text{mart} 1}$	$U_{\text{mart} 3}$	(6:8)	$U_{\text{mart} 6}$	$U_{\text{mart} 8}$
(2:4)	$U_{\text{mart} 2}$	$U_{\text{mart} 4}$	(9:11)	$U_{\text{mart} 9}$	$U_{\text{mart} 11}$
(5:7)	$U_{\text{mart} 5}$	$U_{\text{mart} 7}$	(10:12)	$U_{\text{mart} 10}$	$U_{\text{mart} 12}$

The corresponding habit planes are all crystallographically equivalent.

about 3° from the habit plane (441) reported by Bowles (1951) for this metal (see also Krystian and Pichl, 2000).

6.3. Stacking faults in M9R–M18R martensites

The stretch U_{6M1} given in (3.1) corresponds, in our framework, to the average stretch of (1:3)-twin layering with the exact volume fraction $\frac{1}{3}$. This gives the perfect stacking sequence $++-+-\dots$, i.e., the M9R–M18R martensitic structure as in Fig. 3(a). From (6.6)₁, however, we see that $\frac{1}{3}$ is not the correct proportion needed for compatibility of the (1:3)-twin with the austenite in $\text{CuZn}_{15}\text{Al}_{17}$. When there is twinning at the atomic scale, the value of the phase fraction in (6.6)₁ is realized in this alloy by adding suitable stacking faults to the perfect M9R–M18R sequence. Since

$$\lambda_1 = 0.3225 \approx \frac{1}{3} - \frac{1}{92}, \quad (6.7)$$

the M18R martensite of $\text{CuZn}_{15}\text{Al}_{17}$ needs a stacking-fault density of about one plane in 90 to achieve compatibility. As the stacking-fault density depends on strain (i.e., on lattice parameters) as prescribed by formula (6.4), we can estimate the fault density also in all the other materials of Table 5. The results are shown in Table 6, and can be checked against further experimental fault data, which are currently scarce. We see the computed values are in line with the observation of one fault for every few M18R cells in memory alloys (Chakravorty and Wayman, 1977; Lovey, 1987; Wu et al., 1994), but they underestimate the stacking-fault probability in Li and Na reported by Berliner et al. (1989).⁶ The approximate stacking-fault formula derived by Lovey (1987) gives results that are numerically very close to (6.4).

6.4. Comparison with the 6C ↔ 6M1 kinematics

The numerical value of the stretch matrix U_{mart} in (6.6) differs but in a minor way from the one U_{6M1} obtained in (3.1) through the 6C ↔ 6M1 mechanism (this is schematically represented in Fig. 4). The discrepancy between U_{6M1} and U_{mart} is due to the stacking faults that are necessary for the 6M1 (i.e., M9R–M18R) martensite to achieve

⁶When the phase fraction λ is less than $\frac{1}{3}$, as in (6.7), it means there is less variant 3 in the 1M-twinning than in the ideal case, i.e., more plus signs in the sequence than in the ideal case $++-+-\dots$. These faults thus are of the ‘fcc’ type. In the opposite case they are of the ‘hcp’ type (also called of the 2H type). See Table 6 for a list of values.

compatibility with the austenite, which are taken into account in U_{mart} but not in $U_{6\text{M1}}$. This is also reflected in the fact that the middle eigenvalue μ_2 of U_{mart} is equal to 1 (as prescribed by (5.2)), while this is not so for $U_{6\text{M1}}$. The difference is indeed small for all the materials in Table 5; in Table 6 we list the middle eigenvalue $\mu_2^{6\text{M1}}$ of $U_{6\text{M1}}$ and the corresponding stacking-fault density.

The fact that $\mu_2^{6\text{M1}}$ is always close to 1 is at the origin of the proposal by Hane (1999) to consider the correspondence $6\text{C} \leftrightarrow 6\text{M1}$ for the cubic-to-monoclinic CuZnAl transformation. In the analysis of Hane (1999), the stacking faults are (approximately) accounted for by adjusting the monoclinic angle $\theta_{6\text{M1}}$ so as to make the equality $\mu_2 = 1$ hold exactly, and this variable is thereby eliminated from the theory. In our framework based on the microstrain $U_{1\text{M}}$, such an adjustment is not necessary, as the correct fault density directly arises from the compatibility conditions producing the mesoscale U_{mart} ; the analogous θ_{mart} of $\theta_{6\text{M1}}$ is eliminated altogether here, because $\mu_2 = 1$ always holds for U_{mart} .

6.5. A second habit-plane solution

A second (1:3)-twin exists, also compound, reciprocal to the one considered in Section 6.1 (see Table 1); its elements are $K_1(0\ 1\ 1)$, $\eta_1[0\ \bar{1}\ 1]$, $K_2(0\ \bar{1}\ 1)$, $\eta_2[0\ 1\ \bar{1}]$. One can check that the general expression for the volume fraction $\bar{\lambda}_1$ in this twin can be obtained from the one in (6.2) by exchanging $\alpha_{1\text{M}}$ and $\gamma_{1\text{M}}$. The average stretch, say \bar{U}_{mart} , obtained from this twin is distinct in principle from U_{mart} , and, in general, one should consider that a second series of variants $\bar{U}_{\text{mart}1}, \dots, \bar{U}_{\text{mart}12}$ is possible for the material, besides the series in Table 2. However, these two reciprocal twin systems do not give a truly different adaptive martensitic structure. Indeed, for CuZn₁₅Al₁₇ the second twin gives $\bar{\lambda}_1 = 0.2923$, which is close enough to the value in (6.7) found through the first (1:3)-twin (the amount of martensitic stacking-fault density is predicted for this twin system to be $\frac{1}{24}$). Likewise for the habit plane, and for the martensitic average stretch \bar{U}_{mart} , which are also found to be very close to the analogous quantities for the first twin. One can show that when $\sigma_{1\text{M}} = 0$ the two series of average stretches $U_{\text{mart}1}, \dots, U_{\text{mart}12}$ and $\bar{U}_{\text{mart}1}, \dots, \bar{U}_{\text{mart}12}$ coincide, and so do the M9R–M18R structures they generate. As mentioned in Section 2, the experimental lattice parameters in general do give $\sigma_{1\text{M}} \neq 0$ in our materials, but always by a small value. The adaptive structures obtained through these two twins are therefore practically indistinguishable, with lattice parameters differing by quantities that are within the experimental error. For this reason in what follows we no longer consider this second solution.

6.6. Twinning modes in the M9R–M18R martensite

Before concluding this section, we calculate explicitly the mesoscale twin systems arising in the faulted M9R–M18R martensite. They are given by the solutions to the twinning equation (5.1), when U_{mart} and its variants are considered as the transformation stretches. As mentioned earlier, such variants are of the same monoclinic type as in (4.3); consequently the resulting twins fall into the same seven families indicated in Section 5.2. The corresponding elements must however be given in terms of their indices in the standard M18R cell of Fig. 2, as the experimental data always use this indexing convention. This information for the type-I, -II, and compound twins is summarized in Table 3, together with the corresponding experimental observations, which are well matched by the calculated results.

Table 3

Calculated elements for the transformation twins in the M9R–M18R martensite, indexed in the standard M18R-martensitic cell

Set of twins	Twinning elements indexed in the M18R cell				Experimental observations
	K_1	η_1	K_2	η_2	
S'_c	(10 $\bar{8}$)	[801]	(1010)	$[\bar{1}001]$	Schroeder and Wayman (1977) ^a , Adachi et al. (1986a), Hsu et al. (1999) ^a Tas et al. (1973), Schroeder and Wayman (1977) ^a , Saburi and Nenno (1982), Hsu et al. (1999) ^a
	(1010)	$[\bar{1}001]$	(10 $\bar{8}$)	[801]	
S''_c	(101)	$[\bar{1}01]$	(001)	[100]	Adachi et al. (1986a), Yang et al. (1986) Saburi and Nenno (1981, 1982), Yang et al. (1986)
	(001)	[100]	(101)	$[\bar{1}01]$	
S'_t	(1210)	Irrat.	Irrat.	[891]	Saburi and Nenno (1981, 1982)
	Irrat.	[891]	(1210)	Irrat.	
S''_t	($\bar{1}28$)	Irrat.	Irrat.	$[\bar{1}091]$	Tas et al. (1973), Saburi and Nenno (1982), Andrade et al. (1982), Lovey et al. (1985, 1986), Schroeder and Wayman (1977) ^a , Saburi and Wayman (1979), Saburi and Nenno (1982), Adachi et al. (1986b) Adachi et al. (1986b)
	Irrat.	$[\bar{1}091]$	($\bar{1}28$)	Irrat.	

Also reported are the corresponding observations in the literature.

^aIndicates data originally given through M9R-cell indices, whose relation to the M18R indices is: $(LMN)_{M18R} = (2LMN)_{M9R}$. For both cells the relation $(LMN) = (L\bar{M}N)$ holds, due to symmetry.

7. The wedge microstructure

We can now analyze a typical martensitic microstructure, i.e., the ‘wedge’ observed for instance in $\text{CuZn}_{13.3}\text{Al}_{17.2}$, as shown in Fig. 6 taken from Saburi and Wayman (1979). For M18R martensites it was calculated that the known lattice parameters of Cu-based alloys do not allow for wedge compatibility (K. F. Hane, private communication, and see Table 5 in James and Hane, 2000). We must thus consider that stresses are present in these microstructures so that compatibility be achieved.

7.1. Wedge compatibility in M9R–M18R martensites

The existence of a wedge microstructure at zero stress is given by the following conditions (Bhattacharya, 1991; Hane and Shield, 1998), which include the compatibility equations for the interfaces in Fig. 7:

$$\left\{ \begin{array}{l} R_i U_i - 1 = b_i \otimes \hat{m}_i, \\ R_j U_j - 1 = b_j \otimes \hat{m}_j, \\ R_j U_j - R_i U_i = a \otimes \hat{n}, \\ \hat{m}_i, \hat{m}_j, \hat{n} \text{ coplanar.} \end{array} \right. \quad (7.1)$$

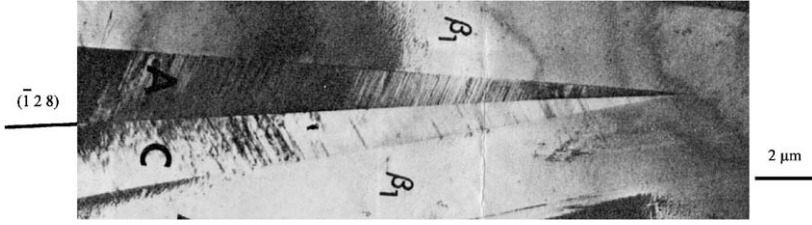


Fig. 6. Wedge microstructure observed in $\text{CuZn}_{13.3}\text{Al}_{17.2}$, from Saburi and Wayman (1979).

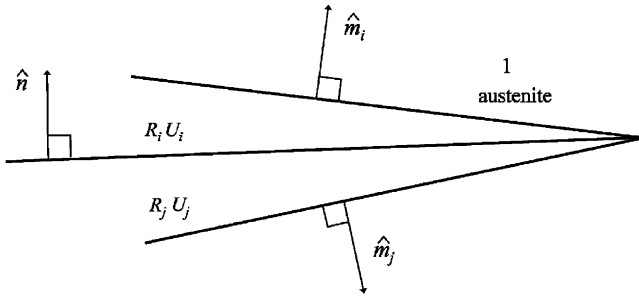


Fig. 7. Deformation gradients in the wedge microstructure.

In our case the transformation stretches U_i and U_j in (7.1) are chosen among the variants of the stretch U_{mart} given in (4.3).

Following Bhattacharya (1991), conditions (7.1) admit solutions if and only if b_i is parallel to b_j , and \hat{m}_i is not parallel to \hat{m}_j . Once the coplanarity of the vectors \hat{m}_i , \hat{m}_j and \hat{n}_i is verified, one checks under which conditions b_i and b_j are parallel. This is done in four cases for each couple $(i : j)$, and may give restrictions on the stretch parameters in U_{mart} . Table 4 shows the result of this analysis performed on all the couples of variants of U_{mart} giving wedges through the twins in Table 3. We find that only the twin systems S'_i and S''_i admit wedge solutions, when suitable relations are satisfied (Table 4), whose easiest expression is given in terms of the quantities

$$\begin{aligned} \alpha_{\text{mart}} &= \frac{|U_{\text{mart}}\tilde{e}_1|}{|\tilde{e}_1|} = \alpha_{6M1} = \alpha_{1M}, \\ \beta_{\text{mart}} &= \frac{|U_{\text{mart}}\tilde{e}_2|}{|\tilde{e}_2|} = \beta_{6M1} = \beta_{1M}, \\ \gamma_{\text{mart}} &= \frac{|U_{\text{mart}}\tilde{e}_3|}{|\tilde{e}_3|} \neq \gamma_{6M1} \neq \gamma_{1M}. \end{aligned} \quad (7.2)$$

7.2. A non-compatibility indicator

The wedge restrictions on stretch parameters given in Table 4 are not verified by the materials in Table 5. One way to measure how far a crystal is from meeting such conditions

Table 4

Restrictions on the stretch parameters in (7.2) allowing for a compatible wedge microstructure in M9R–M18R martensites (type-I, -II, or compound twins only)

Set of twins	Wedge compatibility	Restrictions for wedge compatibility
S'_c	Not possible	
S''_c	Not possible	
S'_t	Possible with type-I twins	$\sqrt{2}\sqrt{\alpha_{\text{mart}}^2 + \gamma_{\text{mart}}^2 - 1}\sqrt{1 - \beta_{\text{mart}}^2} + \beta_{\text{mart}}(\sqrt{\gamma_{\text{mart}}^2 - 1} - \sqrt{\alpha_{\text{mart}}^2 - 1}) = 0$ or $\sqrt{2}\sqrt{\alpha_{\text{mart}}^2 + \gamma_{\text{mart}}^2 - 1}\sqrt{1 - \beta_{\text{mart}}^2} - \beta_{\text{mart}}(\sqrt{\gamma_{\text{mart}}^2 - 1} - \sqrt{\alpha_{\text{mart}}^2 - 1}) = 0$
S''_t	Possible with type-I twins	$\sqrt{2}\sqrt{\alpha_{\text{mart}}^2 + \gamma_{\text{mart}}^2 - 1}\sqrt{1 - \beta_{\text{mart}}^2} - \beta_{\text{mart}}(\sqrt{\gamma_{\text{mart}}^2 - 1} + \sqrt{\alpha_{\text{mart}}^2 - 1}) = 0$

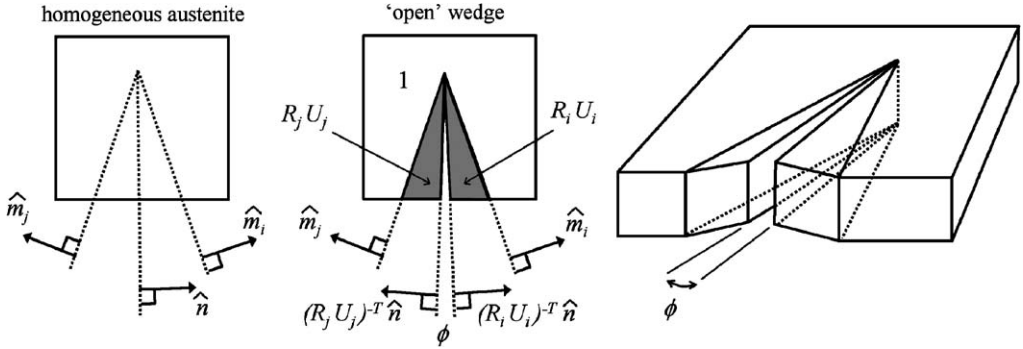


Fig. 8. The angle ϕ obtained by foregoing the requirement of continuity along the midrib of the wedge. This gives a natural indicator of the degree of non-compatibility in this microstructure.

is to consider the angle between the shear vectors b_i and b_j . Hane and Shield (1999b), for instance, find approximately parallel vectors in two theoretical TiNi wedges, and estimate the elastic energy needed to make such vectors parallel.

Table 6 reports the value of the angle between the vectors b_i and b_j for the materials in Table 5, showing that these vectors are always far from parallel; this leads to the conclusion in James and Hane (2000) that the wedge microstructure is not possible in our metals. The fact that wedges do indeed occur in CuZnAl alloys, as in Fig. 6, is therefore not well accounted for by the large values of such angle (b_i, b_j). As a more significant way to measure the amount of non-compatibility, we consider the angle ϕ obtained by ‘releasing’ the midrib interface between the two martensitic variants forming the wedge, see Fig. 8. This angle, which depends on the lattice parameters of the two phases (or equivalently, on the stretch parameters in (7.2)), is given by

$$\phi = \arcsin\left(\frac{|(R_i U_i)^{-T} \hat{n} \wedge (R_j U_j)^{-T} \hat{n}|}{|(R_i U_i)^{-T} \hat{n}| |(R_j U_j)^{-T} \hat{n}|}\right) = \phi(\alpha_{\text{mart}}, \beta_{\text{mart}}, \gamma_{\text{mart}}). \quad (7.3)$$

Notice the monoclinic parameter θ does not influence ϕ , because θ is eliminated through condition (5.2) which holds for U_{mart} . The calculated values of ϕ are reported in Table 6

where one can see that unlike the angle between (b_i, b_j) , ϕ can be quite small in our materials. This suggests that compatibility may be reached in the wedges through small elastic strains and moderate stress levels. We investigate this below, through a three-dimensional finite-element computation using Ansys7.1.

7.3. The stressed wedge

The wedge in Fig. 6 has an $(\bar{1}, 2, 8)_{M18R}$ midrib; comparing with Table 3, we identify its M18R martensitic variants as those pertaining to a type-I twin in family S_t'' , i.e., variants (1:11); for these, Table 6 gives $\phi = 0.32^\circ$. Notice in the same table that the only other possible wedge (the one relating to twin system S_t') has a non-compatibility angle ϕ that is much larger than the S_t' -wedge. This suggests the S_t' -wedge should not form in the material, and goes well with the fact that the $(\bar{1}, 2, 8)_{M18R}$ -midrib wedge is the only one reported in the experimental work on CuZnAl.

The stress-free reference configuration that we take for the finite-element code is the ‘open’ (1:11)-wedge sketched in Fig. 8, in which continuity at the midrib is not enforced. Fig. 9 presents this and the mesh geometry. The computations are done under the hypothesis of linear anisotropic elastic behavior in both the austenite and martensite. The cubic austenite has three independent elastic constants, the monoclinic martensite has 13; their values in both phases of $\text{CuZn}_{12.8}\text{Al}_{17.6}$ have been determined by González-Comas et al. (1997). We take them to be typical of the CuZnAl system (see also Rodríguez et al., 1993).

No external load is applied to the structure, except at the interfaces of the midrib gap. As in the classical ‘Volterra dislocations’ (Love, 1944; Barber, 1992), internal stresses develop in the crystal as the gap is closed by the code in a procedure according to which, using a symmetric mesh, two symmetric nodes, each located on one of the two planes that will meet at the midrib, reach the same position. Due to the crystal anisotropy and the different orientations of the lattices in the two sides of the wedge, the final position of the midrib may not be symmetric with respect to the sides. Fig. 10 shows the stress levels in the wedge obtained in this way. Based on these data, we can also estimate at about 1.3 J/cm^3 the average elastic energy density in this CuZnAl microstructure, which is about 2% of the latent heat of the transformation in this alloy (Peyroux et al., 1998).

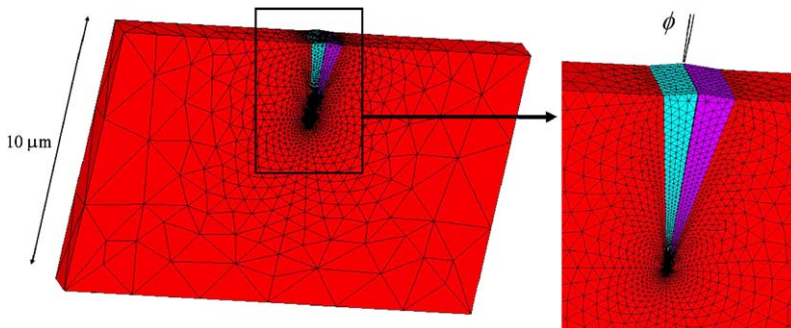


Fig. 9. (Color online). ‘Open’ stress-free reference state for the wedge, and the mesh used in the finite-element calculation. The length of the wedge is $3 \mu\text{m}$, its thickness is $1 \mu\text{m}$. The slab is oriented orthogonally to the vectors \hat{m}_i and \hat{m}_j of formulas (7.1).

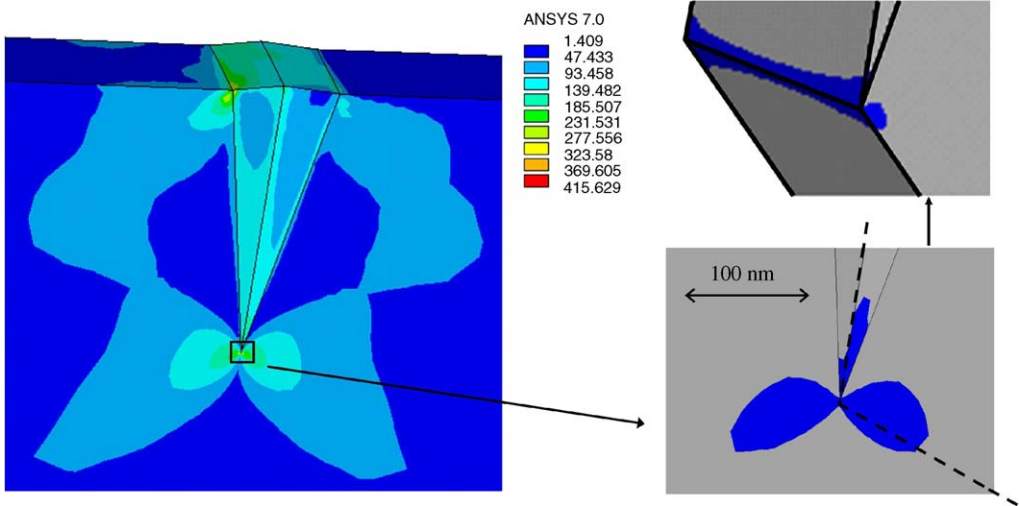


Fig. 10. (Color online). Left panel: stress field in the wedge, indicated by the level curves for the Tresca stress (largest difference among the principal stresses, in MPa) in the crystal. Right panel: the zone where the plastification limit is reached (dark area), shown near the tip and in the interior of the wedge.

Further information can be gleaned from our non-homogeneous stress computation. Indeed, it is natural to compare the stress field with the elastic limits in each phase, to detect the regions of ‘low’ stresses where the crystal remains in the elastic regime, while it may undergo plastification and damage in the rest of the microstructure. This is shown in Fig. 10. The elastic limits of the cubic and monoclinic phases of CuZnAl are unfortunately not very well investigated. Some estimates for (isotropic) CuZnAl polycrystals give between 150 and 300 MPa for the tensile elastic limit in these materials (Van Humbeeck and Delaey, 1989). Other estimates indicate about 350 MPa for the austenite and about 80 MPa for the martensite of a memory CuZnAl (Wu, 1990). The literature thus shows great variation, and we take these values only as an indication of the order of magnitude of the limit for both CuZnAl phases. For the sake of definiteness, in our computations we set the tensile elastic limit at 200 MPa for both austenite and martensite.

In the two right panels of Fig. 10, we have darkened the regions near the wedge tip where the Tresca stress (largest difference among the eigenvalues of the stress tensor) is higher than 200 MPa. This gives a rough estimate of the domains where plastification may occur. The results show that the stresses in the wedge are in general very low, with high values observed only in a very small zone, sized at most at 100 nm, near the tip. We notice this is still an over-estimate of the plastic zone, because stress relief would follow any initial plastic flow of the crystal, and could also occur through the nucleation of other martensitic microstructures near the wedge tip (as is clearly shown for instance in Tan and Xu, 1990), or through an adjustment of the stacking-fault density in the martensite. A more accurate estimate the plastic zone might be obtained by building into the finite-element code an appropriate but much more involved computation of the maximum Schmid stress over the slip systems active in the martensite. This is likely to give very valuable insight when studying plastification in general-stressed microstructures. However, our cruder analysis based on the Tresca stress already indicates the small scale of the zone in the observed

CuZnAl wedge. Analogously to the case of crack modelling, mesh refinement does affect the result of the computations near the tip, but this does not influence our conclusion, as the stresses at any given distance from the tip are well captured by suitable mesh refinement. Our estimate of the magnitude of the plastic zone does suffer, however, from the uncertainty in the values of the anisotropic elastic limit in this material. We also notice that due to the small scale of the plastification domain, the energy dissipated at the tip due to plastic deformation is negligible when compared to the latent heat of the transformation.

7.4. Final remarks

In conclusion, we find that the wedge does indeed require special conditions on the lattice parameters to form coherently at zero stress, but it is observed experimentally in CuZnAl because it can develop under mild stresses. We remark that, as estimated above, the elastic energy needed to make the CuZnAl wedge compatible, when compared to the latent heat, matches the corresponding small ratios found for two theoretical TiNi wedges in Hane and Shield (1999b). However, it is observed that unlike with CuZnAl, no wedges have ever been reported in TiNi. The fact that these microstructures become theoretically compatible in both CuZnAl and TiNi with the addition of amounts of elastic energy which are small compared to the latent heat is thus not enough to clarify actual wedge admissibility. Our computation of the plastic zone shows the latter is small in the CuZnAl wedge. This is a further element indicating that in these alloys this microstructure can play its role as main pathway for the phase change: its imperfect coherence should not hinder the transformation nor its long-term reversibility, as required by good shape-memory performance.

A very interesting point is that the low stresses in the wedge do not sensibly depend on the specific lattice parameters of the alloy considered above. This can be seen by calculating the angle ϕ , which is a good proxy of the microstructure stress, for all the materials in Table 5. We find no great variations of ϕ , and hence of wedge stresses, as a function of lattice (or stretch) parameters (see Table 6). An expressive representation of this is given in Fig. 11, where we show the surface giving ϕ as a function of the stretch parameters α_{mart} and γ_{mart} in (7.2). The stretch β_{mart} is kept fixed to allow for a plot in three dimensions; changing the value of β_{mart} within an interval compatible with the experimental data does not alter the picture. We see that the valley surrounding the perfect-compatibility line $\phi = 0$ is quite flat, making imperfect wedge compatibility easy to accommodate in a wide range of lattice parameters. The materials in Table 5, represented by black dots on the surface, lie indeed on the flat valley bottom away from the line $\phi = 0$. In the case of CuZnAl, although the available data do not evenly cover the domain \mathcal{D} of compositions where this alloy admits the cubic-to-monoclinic transformation, we conjecture the wedge stresses remain low in a wide portion of \mathcal{D} . The neighborhood of the special relations (in both lattice-parameter and composition spaces), where the wedge is still admissible, thus appears quite large in these materials. This may contribute to explain why CuZnAl alloys exhibit good shape memory in a broad range of compositions without having to satisfy special lattice-parameter relations (such as for wedge compatibility) too closely. It is an interesting task, left for further work, to check whether analogous conclusions may hold also for other classes of memory materials, and for other morphologies typically exhibited by such substances.

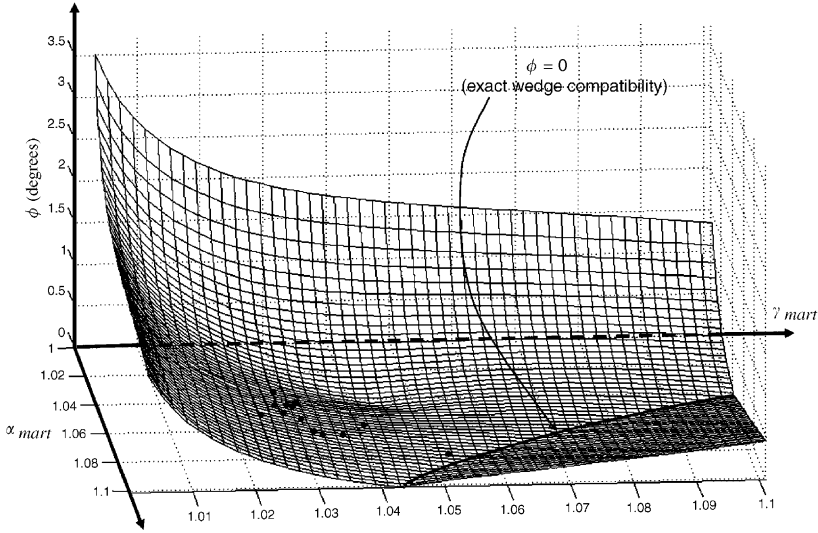


Fig. 11. Surface showing the value of the wedge non-compatibility indicator ϕ in (7.3) as a function of the stretch parameters in (7.2), for fixed $\beta_{mart} = 0.9055$. This gives an explicit representation of the average stress levels in the wedge as a function of lattice parameters. Notice the wide flat valley that surrounds the line $\phi = 0$ where there is wedge compatibility. The black dots, representing the stretch parameters of the materials in Table 5, all lie on the flat spot of the surface.

Acknowledgments

Both authors were partially supported by the Marie Curie contract MRTN-CT-2004-505226 ‘MULTIMAT’ of the European Union. G.Z. was also partially supported by the ‘Mathematical Nanomechanics’ program of INDAM, Italy.

Appendix A

A.1. The bcc-to-9R transformation

Geometrically, the (no-color) monoclinic structure M9R–M18R is but a slight deformation of the (close-packed) rhombohedral 9R structure (Strukturbericht C19, 1928–1932), so that the bcc-to-M18R transformation is a distorted version of the well-known bcc-to-9R phase change. The basic mechanism of the latter, is, in turn, the same as for any bcc-to-close-packed transformation.⁷

In detail, the close-packing of an originally bcc structure occurs as follows. Consider the bcc lattice (whose atoms are assumed to be all equal-radius spheres) as constituted by the alternate layering of the crystallographic planes A and B in Fig. 1, with indices $(\bar{1}01)_{bcc}$. On these planes (which are the densest in the bcc lattice) the atoms form nets of rhombi

⁷We recall the bcc-to-9R is but one of the several transformations from an ‘open’ bcc to a close-packed structure that are observed in nature. Many elemental crystals, for instance, undergo such transformations, and in particular, the bcc-to-9R transition occurs in Ag, Li, Na, Sm. See Table 5 for some data.

whose small angles are about 71° . Then, the close-packing mechanism (in the ideal case) consists of these basic two steps (Burgers, 1934; Nishiyama, 1978):

- (I) The nets of atoms on the A–B planes go to a close-packed configuration undergoing a contraction along $[010]_{\text{bcc}}$ and an elongation along $[101]_{\text{bcc}}$. On each plane this reduces from about 70.2° to 60° the angle of the rhombic nets of atoms, with lattice parameter a_h .
- (II) Correspondingly, a suitable relative sliding of adjacent A–B planes achieves a densest stacking arrangement. This is done through a shear along $[101]_{\text{bcc}}$ (two opposite directions are possible, with amplitude exactly $a_h/6$), and an adjustment of the interplanar distance to attain three-dimensional close-packing.

The stacking sequence produced by this ‘zig-zag’ sliding characterizes the structure of the final close-packed crystal, and infinitely many periodic and non-periodic sequences are possible a priori. The best-known periodic sequences, observed under different conditions in many elements, are the fcc and the hcp structures. They are characterized by the stacking sequences ABCABC... and ABABAB..., respectively. Also the close-packed 9R structure is periodic, being obtained from the sequence ABCBCACAB....

The final stacking sequence of close-packed planes in the product phase defines the martensitic ‘mesoscale’ structure, which is decided by the compatibility conditions at the austenite/martensite interface. In this approach the layering patterns producing the long-period stacking M9R–M18R martensites are interpreted as deriving from atomic-scale twinning. From this point of view, the usual characterization of the M9R–M18R martensites as ‘internally twinned’ or ‘microtwinning’ (rather than ‘untwinned’ as in Hane, 1999; James and Hane, 2000) is very natural. See Gooding and Krumhansl (1988), Khachatryan et al. (1991), and Blaschko et al. (1999) for some discussion of the energetics of long-period stacking martensites and very fine atomic-scale layering.

Various other, more complex ‘polytype’ or ‘modulated’ martensitic structures are known to arise from the bcc-to-compact transformation, exhibiting different orderings and faulting in the stacking sequences of the close-packed planes. The possibility that the formation of the 9R or other such complex structures be due to the reduction of coherence stresses at the austenite/martensite interface has been discussed by several authors: see for instance Blaschko et al. (1988), Schwarz and Blaschko (1990), Smith et al. (1990), Schwarz et al. (1991, 1992), Berliner et al. (1992), and Krystian and Pichl (2000). See also Maier et al. (1995, 1997a, b) and Blaschko et al. (1999) for work regarding the influence of imposed loads affecting the stresses at the austenite/martensite interface.

A.2. Summary of formulas

Lattice parameters: The parameters of the cells 6M1 and 1M in terms of the parameters of the M18R or M9R cells are given by

$$\begin{cases} \theta_{6M1} = \pi - \arctan \frac{c_{M18R} \sin \theta_{M18R}}{a - c_{M18R} \cos \theta_{M18R}} = \pi - \arctan \frac{2c_{M9R} \sin \theta_{M9R}}{a - 2c_{M9R} \cos \theta_{M9R}}, \\ c_{6M1} = \frac{c_{M18R} \sin \theta_{M18R}}{3 \sin \theta_{6M1}} = \frac{2c_{M9R} \sin \theta_{M9R}}{3 \sin \theta_{6M1}} \end{cases} \quad (\text{A.1})$$

and

$$\begin{cases} \theta_{1M} = \pi - \arctan \frac{c_{M18R} \sin \theta_{M18R}}{3a - 3c_{M18R} \cos \theta_{M18R}} = \pi - \arctan \frac{2c_{M9R} \sin \theta_{M9R}}{3a - 6c_{M9R} \cos \theta_{M9R}}, \\ c_{1M} = \frac{c_{M18R} \sin \theta_{M18R}}{18 \sin \theta_{1M}} = \frac{c_{M9R} \sin \theta_{M9R}}{9 \sin \theta_{1M}}. \end{cases} \quad (A.2)$$

Entries for the stretch matrix U_{1M} : The values of β_{1M} , ρ_{1M} , σ_{1M} and τ_{1M} in (3.3) are obtained from the lattice parameters of the 1M cell through the following formulas:

$$\begin{cases} \rho_{1M} = \frac{\alpha_{1M}^2 + \gamma_{1M}^2 + 2\alpha_{1M}\gamma_{1M}(\sin \theta_{1M} + \cos \theta_{1M})}{2\sqrt{\alpha_{1M}^2 + \gamma_{1M}^2 + 2\alpha_{1M}\gamma_{1M} \sin \theta_{1M}}}, \\ \tau_{1M} = \frac{\alpha_{1M}^2 + \gamma_{1M}^2 + 2\alpha_{1M}\gamma_{1M}(\sin \theta_{1M} - \cos \theta_{1M})}{2\sqrt{\alpha_{1M}^2 + \gamma_{1M}^2 + 2\alpha_{1M}\gamma_{1M} \sin \theta_{1M}}}, \\ \sigma_{1M} = \frac{\alpha_{1M}^2 - \gamma_{1M}^2}{2\sqrt{\alpha_{1M}^2 + \gamma_{1M}^2 + 2\alpha_{1M}\gamma_{1M} \sin \theta_{1M}}} \end{cases} \quad (A.3)$$

Table 5

Lattice parameters for materials exhibiting long-period stacking monoclinic martensites (in Angstroms and degrees; compositions are in at%)

Alloy (at%)	Ref.	Transition type	Lattice parameters					
			Austenite		Martensite			
			a		a	b	c	θ
CuZn ₁₅ Al ₁₇	Chakravorty and Wayman (1977)	DO ₃ /M18R	5.996		4.553	5.452	38.977	87.5
CuZn _{14.6} Al _{16.1}	Adachi and Perkins (1986)	DO ₃ /M18R	5.843		4.430	5.304	38.012	88.9
CuZn _{24.75} Al _{9.32}	Zhu et al. (1989)	B2/M9R	2.939		3.6783	2.5998	19.1277	89.5
CuZn _{26.6} Al _{7.06}	Eon and Yong (1990)	B2/M9R	2.94		4.52	2.64	19.18	89
CuZn _{24.7} Al ₁₁	Yang et al. (1986)	DO ₃ /M18R	5.87		4.45	5.27	38.66	89
CuZn _{23.73} Al _{9.4}	Lexcellent et al. (2002)	DO ₃ /M18R	5.870(4)		4.441(4)	5.330(4)	38.13(2)	89.08
CuZn _{24.7} Al ₉	Wu et al. (1994)	B2/M9R	2.94		4.41	2.67	19.18	89
CuZn _{22.48} Al _{2.58}	Morin (1985)	DO ₃ /M18R	5.846		4.405	5.34	38.260	87.5
CuZn _{37.65}	Kajiwara and Kikuchi (1982)	B2/M9R	2.92		4.41	2.68	19.20	88.4
CuZn _{39.3}	Saburi and Wayman (1979)	B2/M9R	2.94		4.412	2.678	19.19	88.5
CuZn ₂₀ Ga ₁₂	Saburi et al. (1976)	DO ₃ /M18R	5.86		4.40	5.33	38.22	88.33
CuAl ₁₄ Ni ₄	Tokonami et al. (1979)	DO ₃ /M18R	5.836		4.430	5.330	38.19	89.0
CuAl ₁₁ Be ₂	Satto and Lexcellent (2001)	DO ₃ /M18R	5.827		4.57	5.34	38.8	88.3
CuAl ₁₀ Zn ₅ Mn ₅	Sittner et al. (2000)	DO ₃ /18R	5.87		4.44	5.36	38.22	90
Li	Berliner et al. (1989)	A2/9R	3.47851(1)		$\sqrt{3}b$	3.1010(3)	22.7649(2)	90
	Smith (1987)	A2/9R	3.483(2)		$\sqrt{3}b$	3.103(2)	22.797	90
Na	Berliner et al. (1989)	A2/9R	4.22140(2)		$\sqrt{3}b$	3.76586(8)	27.6531(2)	90

The values of a [a , b , c , θ] for the cubic austenite [monoclinic martensite] refer to the standard austenitic cell A2, B2, DO₃1, L2₁ [martensitic cells 9R, M9R, 18R, M18R], as indicated under 'transition type' (see Section 2). The very low value of a for martensitic CuZn_{24.75}Al_{9.32} is doubtful.

and

$$\alpha_{1M} = \frac{|U_{1M}e_1|}{|e_1|} = \frac{\sqrt{2}a_{1M}}{2a_{bcc}}, \quad \beta_{1M} = \frac{|U_{1M}e_2|}{|e_2|} = \frac{b_{1M}}{a_{bcc}}, \quad \gamma_{1M} = \frac{|U_{1M}e_3|}{|e_3|} = \frac{2c_{1M}}{\sqrt{2}a_{bcc}}. \quad (\text{A.4})$$

Twinning solutions: When they exist, the two solutions of Eq. (5.1) are given by the following expressions:

$$\hat{n} = \frac{1\sqrt{\mu_3} - \sqrt{\mu_1}}{\chi\sqrt{\mu_3 - \mu_1}}(-\sqrt{1 - \mu_1}F_1^T\hat{v}_1 + \kappa\sqrt{\mu_3 - 1}F_1^T\hat{v}_3), \quad (\text{A.5})$$

$$a = \frac{\chi}{\sqrt{\mu_3 - \mu_1}}(\sqrt{\mu_3(1 - \mu_1)}\hat{v}_1 + \kappa\sqrt{\mu_1(\mu_3 - 1)}\hat{v}_3),$$

where \hat{v}_1 and \hat{v}_3 are the unit eigenvectors of C corresponding to the eigenvalues μ_1 and μ_3 , respectively (see (5.2)). Here $\kappa = \pm 1$ (the two options giving ‘conjugate solutions’), and χ is a non-zero constant, used to make \hat{n} a unit vector.

Table 6
Summary of calculated data for the materials listed in Table 5

Material	Angle (b_i, b_j) with type-I twins		Non-compatibility angle ϕ with type-I twins		λ (s.f.d.)	μ_2^{6M1}	$\det U$
	S'_i set (deg.)	S''_i set (deg.)	S'_i set (deg.)	S''_i set (deg.)			
CuZn ₁₅ Al ₁₇	47.0	8.5	7.0	0.32	0.3225 (1/92 fcc)	1.0019	0.9964
CuZn _{14.6} Al _{16.1}	48.5	8.7	7.4	0.31	0.3632 (1/33 hcp)	0.9926	0.9948
CuZn _{24.75} Al _{9.32}	No sol.	No sol.	No sol.	No sol.	No sol.	0.8846	0.8006
CuZn _{26.6} Al _{7.06}	47.4	7.9	8.3	0.34	0.3447 (1/88 hcp)	0.9972	1.0006
CuZn _{24.7} Al ₁₁	54.8	7.7	9.9	0.19	0.3305 (1/350 fcc)	1.0008	0.9915
CuZn _{23.73} Al _{9.4}	48.7	9.3	7.2	0.35	0.3738 (1/25 hcp)	0.9896	0.9915
CuZn _{24.7} Al ₉	53.6	10.2	7.9	0.25	0.3675 (1/29 hcp)	0.9909	0.9873
CuZn _{22.48} Al _{2.58}	51.4	6.1	7.7	0.16	0.3033 (1/33 fcc)	1.0057	1.0001
CuZn _{37.65}	51.2	2.1	8.0	0.05	0.3204 (1/77 fcc)	1.0031	1.0123
CuZn _{39.3}	52.9	8.9	7.8	0.22	0.3529 (1/51 hcp)	0.9953	0.9910
CuZn ₂₀ Ga ₁₂	52.7	9.6	7.7	0.25	0.3498 (1/61 hcp)	0.9962	0.9894
CuAl ₁₄ Ni ₄	48.9	4.2	7.7	0.13	0.3467 (1/75 hcp)	0.9965	1.0080
CuAl ₁₁ Be ₂	43.6	7.6	8.9	0.39	0.2344 (1/10 fcc)	1.0226	1.0630
CuAl ₁₀ Zn ₅ Mn ₅	48.5	6.9	7.1	0.22	0.3848 (1/19 hcp)	0.9843	0.9993
Li	48.6	8.0	9.3	0.36	0.3556 (1/45 hcp)	0.9934	1.0009
	49.0	8.3	9.3	0.36	0.3558 (1/45 hcp)	0.9933	0.9998
Na	48.6	7.4	9.3	0.32	0.3526 (1/52 hcp)	0.9943	1.0033

Columns 2–5 refer to the non-compatibility of the wedge microstructure (columns 2–3 indicate the angle between the shear vectors b_i and b_j in Eqs. (7.1), columns 4–5 give the value of the angle ϕ (indicator of non-compatibility) considered in Section 7.2). Column 6 gives the calculated value of the phase fraction λ of variant 3 in the (1:3) IM-martensitic twinning (the corresponding stacking-fault density in the M9R–M18R martensite is also indicated in parenthesis, together with the predominant stacking-fault type, see Section 6.3). Column 7 gives the value of middle eigenvalue μ_2^{6M1} of the stretch U_{6M1} (the value 1 corresponds to zero stacking-fault density in the M9R–M18R martensite). Column 8 gives the value of the determinant of the transformation stretch, which is the same for U_{1M} , U_{6M1} or U_{mart} .

A.3. Summary of lattice parameters and other data

For reference purposes, in Table 5 we report the data on materials exhibiting long-period stacking M9R–M18R martensites, whose complete set of austenitic and martensitic lattice parameters is available. In Table 6, we summarize other relevant data on the same materials, obtained from the analysis in the text.

References

- Adachi, K., Perkins, J., 1986. Deformation of martensite in a polycrystalline Cu–Zn–Al alloy. *Metall. Trans. A* 17A, 945–959.
- Adachi, K., Perkins, J., Wayman, C.M., 1986a. Intervariant transitions without a defined interface in 18R Cu–Zn–Al martensites. In: *Proceedings of the International Conference on Martensitic Transformations*, The Japan Institute of Metals, pp. 838–843.
- Adachi, K., Perkins, J., Wayman, C.M., 1986b. Type II twins in self-accommodating martensite plate variants in a Cu–Zn–Al shape memory alloy. *Acta Metall.* 34, 2471–2485.
- Andrade, M., Delaey, L., Chandrasekaran, M., 1982. On some lesser known planar defects in β'_1 Cu–Zn–Al martensite. *J. Phys. IV*, C4–43.
- Ball, J.M., James, R.D., 1987. Fine phase mixtures as minimizers of energy. *Arch. Ration. Mech. Anal.* 100, 13–52.
- Ball, J.M., James, R.D., 1992. Proposed experimental tests of a theory of fine microstructure and the two-well problem. *Philos. Trans. R. Soc. London A* 338, 389–450.
- Barber, J.R., 1992. *Elasticity*. Kluwer Academic Publishers, Dordrecht.
- Barrett, C.S., Massalski, T.B., 1980. *Structure of Metals*. Pergamon Press, New York.
- Berliner, R., Fajen, O., Smith, H.G., Hitterman, R.L., 1989. Neutron powder diffraction studies of lithium, sodium, and potassium metal. *Phys. Rev. B* 40, 12086–12097.
- Berliner, R., Smith, H.G., Copley, J.R.D., Trivisonno, J., 1992. Structures of sodium metal. *Phys. Rev. B* 46, 14436–14447.
- Bhattacharya, K., 1991. Wedge-like microstructures in martensite. *Acta Mater.* 39, 2431–2444.
- Bhattacharya, K., 2003. *Microstructure of Martensite*. Oxford University Press, Oxford.
- Bhattacharya, K., Conti, S., Zanzotto, G., Zimmer, J., 2004. Crystal symmetry and the reversibility of martensitic transformations. *Nature (London)* 428, 55–59.
- Blaschko, O., Krexner, G., Pleschiutchnig, J., Ernst, G., Hitznerberger, C., Karthaler, H.P., Korner, A., 1988. Coherent modulated structure during the martensitic hcp–fcc phase transition in Co and in a CoNi alloy. *Phys. Rev. Lett.* 60, 2800–2803.
- Blaschko, O., Dmitriev, V., Krexner, G., Toledano, P., 1999. Theory of the martensitic transformations in lithium and sodium. *Phys. Rev. B* 59, 9095–9112.
- Bowles, J.S., 1951. Metallographic study of the martensite transformation in lithium. *Trans. Metall. Soc. AIME* 191, 44–50.
- Bowles, J.S., 1954. The crystallography of martensitic transformation I and II. *Acta Metall.* 2, 129–147.
- Burgers, W.G., 1934. On the process of transition of the cubic-body-centered modification into hexagonal-close-packed modification of zirconium. *Physica (Utrecht)* 1, 561–586.
- Chakravorty, S., Wayman, C.M., 1977. Electron microscopy of internally faulted Cu–Zn–Al martensite. *Acta Metall.* 25, 989–1000.
- Eon, S.L., Yong, G.K., 1990. A transformation kinematic model and its application to Cu–Zn–Al shape memory alloy—I isothermal condition. *Acta Metall.* 38, 1669–1678.
- Ericksen, J.L., 1980. Some phase transitions in crystals. *Arch. Ration. Mech. Anal.* 73, 99–124.
- Ericksen, J.L., 1985. Some surface defects in unstressed thermoelastic solids. *Arch. Ration. Mech. Anal.* 88, 337–345.
- Ernst, F., Finnis, M.W., Hofmann, D., Muschik, T., Schoenberger, U., Wolf, U., Methfessel, M., 1992. Theoretical prediction and direct observation of the 9R structure in Ag. *Phys. Rev. Lett.* 69, 620–623.
- Falk, F., Konopka, P., 1990. Three-dimensional Landau theory describing the martensitic phase transformation of shape memory alloys. *J. Phys.: Condens. Matter* 2, 61–76.

- González-Comas, A., Mañosa, L., Planes, A., Lovey, F.C., Pelegrina, J.L., Guenin, G., 1997. Temperature dependence of the second-order elastic constants of Cu–Zn–Al shape-memory alloy in its martensitic and β phases. *Phys. Rev. B* 56, 5200–5206.
- Gooding, R.J., Krumhansl, J.A., 1988. Theory of the bcc-to-9R structural phase transformation of Li. *Phys. Rev. B* 38, 1695–1703.
- Gui, J., Wang, R., Zhao, Y., 1988. Determination of the effect of heat treatment on the x parameter of 18R₁ martensite in Cu–Zn–Al alloys. *J. Appl. Crystallogr.* 21, 340–348.
- Gurtin, M.E., 1983. Two-phase deformations of elastic solids. *Arch. Ration. Mech. Anal.* 84, 1–29.
- Hane, K.F., 1999. Bulk and thin microstructures in untwinned martensites. *J. Mech. Phys. Solids* 47, 1917–1939.
- Hane, K.F., Shield, T.W., 1998. Symmetry and microstructure in martensites. *Philos. Mag. A* 78, 1215–1252.
- Hane, K.F., Shield, T.W., 1999a. Microstructure in a copper–aluminium–nickel shape-memory alloy. *Proc. R. Soc. London A* 455, 3901–3915.
- Hane, K.F., Shield, T.W., 1999b. Microstructure in the cubic to monoclinic transition in titanium–nickel shape memory alloys. *Acta Mat.* 47, 2603–2617.
- Hane, K.F., Shield, T.W., 2000. Microstructure in the cubic to trigonal transition. *Mater. Sci. Eng. A* 291, 147–159.
- Hsu, Y.F., Wang, W.H., Wayman, C.M., 1999. Microstructure and martensitic transformations in a dual-phase Cu–Zn alloy. *Metall. Mater. Trans. A* 30, 729–739.
- James, J.D., Hane, K.F., 2000. Martensitic transformations and shape memory materials. *Acta Mat.* 48, 197–222.
- James, R.D., Zhang, Z., 2005. A way to search for multiferroic materials with ‘unlikely’ combinations of physical properties. In: Manosa, L., Planes, A., Saxena, A.B. (Eds.), *Interplay of Magnetism and Structure in Functional Materials*. Springer, Berlin, pp. 1–15.
- Kajiwara, S., Kikuchi, T., 1982. Dislocation structures produced by reverse martensitic transformation in a Cu–Zn alloy. *Acta Metall.* 30, 589–598.
- Khachatryan, A.G., Shapiro, S.M., Semenovskaya, S., 1991. Adaptive phase formation in martensitic transformation. *Phys. Rev. B* 43, 10832–10843.
- Krystian, M., Pichl, W., 2000. In situ optical microscopy of the martensitic phase transformation of lithium. *Phys. Rev. B* 62, 13956–13962.
- Lexcellent, C., Blanc, P., 2004. Phase transformation yield surface determination for some shape memory alloys. *Acta Mat.* 52, 2317–2324.
- Lexcellent, C., Vivet, A., Bouvet, C., Calloch, S., Blanc, P., 2002. Experimental and numerical determinations of the initial surface of phase transformation under biaxial loading in some polycrystalline shape-memory alloys. *J. Mech. Phys. Solids* 35, 2717–2735.
- Liu, A.Y., Cohen, M.L., 1991. Electron phonon coupling in bcc and 9R lithium. *Phys. Rev. B* 44, 9678–9684.
- Love, A.E.H., 1944. *A Treatise on the Mathematical Theory of Elasticity*, fourth ed. Dover Publications, New York.
- Lovey, F.C., 1987. The fault density in 9R type martensites: a comparison between experimental and calculated results. *Acta Metall.* 35, 1103–1108.
- Lovey, F.C., Van Tendeloo, G., Van Landuyt, J., Amelinckx, S., 1985. High resolution electron microscopy of twin interfaces in 2H and 18R martensites of Cu–Al alloys. *Scr. Metall.* 19, 1223–1228.
- Lovey, F.C., Van Tendeloo, G., Van Landuyt, J., Amelinckx, S., 1986. High resolution electron microscopy of defects and twin interfaces in 2H and 18R martensite of Cu–Al alloys. In: *Proceedings of the International Conference on Martensitic Transformations*, The Japan Institute of Metals, pp. 762–767.
- Lovey, F.C., Van Tendeloo, G., Van Landuyt, J., 1987. High resolution microscopy imaging of the habit plane in Cu–Zn–Al shape memory alloys. *Scr. Metall.* 21, 1627–1631.
- Maier, Ch., Blaschko, O., Pichl, W., 1995. Influence of uniaxial deformation on the phase transformation in lithium. *Phys. Rev. B* 52, 9283–9290.
- Maier, Ch., Blaschko, O., Pichl, W., 1997a. Influence of plastic deformation on the martensitic phase transformation in lithium. *Phys. Rev. B* 55, 113–116.
- Maier, Ch., Blaschko, O., Pichl, W., 1997b. Influence of small uniaxial strains on the martensitic phase transition in alkali–metal systems. *Phys. Rev. B* 55, 12062–12066.
- Morin, M., 1985. Contribution à l'étude des phénomènes anélastiques liés à la transformation martensitique du CuZnAl. Thèse d'état no I DE 8503, INSA Lyon, France.
- Neaton, J.B., Ashcroft, N.W., 2001. On the constitution of sodium at higher densities. *Phys. Rev. Lett.* 86, 2830–2833.
- Nishiyama, Z., 1978. *Martensitic Transformation*. Academic Press, New York.

- Otsuka, K., Shimizu, K., 1974. Morphology and crystallography of thermoelastic Cu–Al–Ni martensite analyzed by the phenomenological theory. *Trans. Jpn. Inst. Metall.* 15, 103–108.
- Otsuka, K., Wayman, C.M., Nakai, K., Sakamoto, H., Shimizu, K., 1976. Superelasticity effects and stress-induced martensitic transformations in Cu–Al–Ni alloys. *Acta Metall.* 24, 207–226.
- Otsuka, K., Ohba, T., Tokonami, M., Wayman, C.M., 1993. New description of long-period stacking order structures of martensites in β -phase alloys. *Scr. Metall. Mat.* 29, 1359–1364.
- Overhauser, A.W., 1984. Crystal structure of lithium at 4.2 K. *Phys. Rev. Lett.* 53, 64–65.
- Peyroux, R., Chrysochoos, A., Licht, C., Lobel, M., 1998. Thermomechanical couplings and pseudoelasticity of shape memory alloys. *Int. J. Eng. Sci.* 36, 489–509.
- Pitteri, M., 1984. Reconciliation of local and global symmetries of crystals. *J. Elasticity* 14, 175–190.
- Pitteri, M., Zanzotto, G., 1998. Generic and non-generic cubic-to-monoclinic transitions and their twins. *Acta Metall.* 46, 225–237.
- Pitteri, M., Zanzotto, G., 2002. *Continuum Models for Phase Transitions and Twinning in Crystals*. Chapman & Hall, CRC, London, Boca Raton, FL.
- Redfield, A.C., Zangwill, A.M., 1986. Stacking sequences in closed-packed metallic superlattices. *Phys. Rev. B* 34, 1378–1380.
- Rodriguez, P.L., Lovey, F.C., Guenin, J.L., Sade, M., Morin, M., 1993. Elastic constants of the monoclinic 18R martensite of a Cu–Zn–Al alloy. *Acta Mat.* 41, 3307–3310.
- Saburi, T., Nenno, S., 1981. The shape memory effect and related phenomena. In: Aaronson, H.I., Laughlin, D.E., Sekerka, R.E., Wayman, C.M. (Eds.), *Proceedings of the International Conference on Solid–Solid Transformations*, Pittsburgh, PA, August 10–14, pp. 828–831.
- Saburi, T., Nenno, S., 1982. The shape memory effect and related phenomena. In: Aaronson H.I. (Ed.), *Proceedings of the International Conference on Solid–Solid Transformations AIME*, pp. 1455–1479.
- Saburi, T., Wayman, C.M., 1979. Crystallographic similarities in shape memory martensite. *Acta Metall.* 27, 979–995.
- Saburi, T., Nenno, S., Kato, S., Takata, K., 1976. Configurations of martensite variants in Cu–Zn–Ga. *J. Less Common. Metall.* 50, 223–236.
- Satto, C., Lexcellent, C., 2001. Private communication.
- Schroeder, T.A., Wayman, C.M., 1977. The formation of martensite and the mechanism of the shape memory effect in single crystals of Cu–Zn alloys. *Acta Metall.* 25, 1375–1391.
- Schwarz, W., Blaschko, O., 1990. Polytype structures of lithium at low temperature. *Phys. Rev. Lett.* 65, 3144–3147.
- Schwarz, W., Blaschko, O., Gorgas, I., 1991. Bcc instability of lithium at low temperatures. *Phys. Rev. B* 44, 6785–6790.
- Schwarz, W., Blaschko, O., Gorgas, I., 1992. Diffuse-neutron-scattering investigation of the low-temperature phases of sodium. *Phys. Rev. B* 46, 14448–14452.
- Sittner, P., Lukás, P., Daymon, M.R., Novác, V., Swallowe, G.M., 2000. Stress induced martensitic transformation in CuAlZnMn polycrystals investigated by in situ neutron diffraction. In: *ESOMAT 2000*, Como, Italy, September 4–8, pp. 897–902.
- Smith, H.G., 1987. Martensitic phase transformation of single crystal lithium from bcc to a 9R-related structure. *Phys. Rev. Lett.* 58, 1228–1231.
- Smith, H.G., Berliner, R., Jorgensen, J.D., Nielsen, N., Trivisonno, J., 1990. Pressure effects on the martensitic transformation in metallic lithium. *Phys. Rev. B* 41, 1231–1234.
- Strukturbericht, B. II, 1928–1932. In: Niggli et al. P. (Eds.), *Akademische Verlagsgesellschaft M.B.H. Leipzig*. (Reproduced by Edwards Brothers, Ann Arbor, MI, 1943.) Supplement to Z. Kristallogr. Kristallgeom. Kristallphys. Krystalchem. See also: (<http://cst-www.nrl.navy.mil/lattice/struk/>).
- Takezawa, K., Shindo, T., Sato, S., 1976. Shape memory effects in β'_1 Cu–Zn alloys. *Scr. Metall.* 10, 13–18.
- Tan, S., Xu, H., 1990. Observations on a CuAlNi single crystal. *Cont. Mech. Thermodyn.* 2, 241–244.
- Tas, H., Delaey, L., Deruyttere, A., 1973. The self-accommodating character of the β'_1 copper–aluminum martensite. *Metall. Trans.* 4, 2833–2840.
- Tokonami, M., Otsuka, K., Shimizu, K., Iwata, Y., Shibuya, I., 1979. Neutron diffraction studies of crystal structures of stress-induced martensites in a Cu–Al–Ni alloy. In: *Proceedings of the International Conference of Martensitic Transformations*, Cambridge, MA, pp. 639–644.
- Van Humbeeck, J., Delaey, L., 1989. In: Hornbogen, E., Jost, N. (Eds.) *The Martensitic Transformation in Science and Technology* (DGM Informationsgesellschaft), p. 15.
- Wayman, C.M., 1977. *Introduction to the Crystallography of Martensitic Transformations*. Macmillan, New York.

- Wechsler, M.S., Lieberman, D.S., Read, T.A., 1953. On the theory of the formation of martensite. *Trans. Metall. Soc. AIME* 197, 1503–1515.
- Wu, M.H., 1990. In: Duerig, T.W., Melton, K.N., Stockel, D., Wayman, C.M. (Eds.), *Engineering Aspects of Shape Memory Alloys*, Butterworth-Heinemann, London.
- Wu, M.H., Hamada, Y., Wayman, C.M., 1994. Transformation characteristics of α_1 plates in CuZnAl alloys. *Metall. Mater. Trans. A* 25, 2581–2599.
- Yang, D.Z., Zhu, M., Kuo, K.H., 1986. On the crystal structure and substructure of martensites formed in a CuZnAl alloy. In: *Proceedings of the International Conference on Martensitic Transformations*, The Japan Institute of Metals, pp. 828–831.
- Zhu, W.J., Chen, W.Y., Hsu, T.Y., 1989. Group theory and crystallography of the martensitic transformation in Cu–26.71Zn–4.15Al. *Acta Metall.* 33, 2075–2082.